*Master in Quantum Science and Technology*

---

# Circuit Quantum Electrodynamics with Transmon Qubits in the Ultrastrong Coupling Regime

---


**Adrián Parra Rodríguez**

*Advisor:*
**Prof. Enrique Solano**




Department of Physical Chemistry
Faculty of Science and Technology
University of the Basque Country UPV/EHU


Leioa, 15th September 2016

# Declaration of Authorship

I, Adrián Parra Rodríguez, hereby certify that the thesis with the name "Circuit Quantum Electrodynamics with Transmon Qubits in the Ultrastrong Coupling Regime" is entirely my own original work except where otherwise indicated. I am aware of the University's regulations concerning plagiarism, including those regulations concerning disciplinary actions that may result from plagiarism. Any use of the works of any other author, in any form, is properly acknowledged at their point of use.

Signature:

_____

Date:
20th July 2016

# Abstract

We propose a circuit model to describe transmon qubits coupled to multimode transmission line resonators. This model has been developed in the frame of circuit quantum electrodynamics and contrasted with available experimental data, and it might be useful for designing future experiments in extreme coupling regimes. In addition, collapses and revivals of qutrit populations are also observed in an extended version of the quantum Rabi model, in both the ultrastrong and deep strong coupling regimes. This work opens the door for using the transmon-resonator system in quantum simulations or quantum computation processes, where such regimes may enhance the toolbox of already available interactions.

# Resumen

Proponemos un modelo circuital para describir transmones acoplados a resonadores de lineas de transmisión multimodo. Este modelo ha sido desarrollado en el marco de la electrodinámica cuántica con circuitos y contrastado con datos experimentales disponibles, esperando que sea útil para diseñar futuros experimentos en regímenes de acoplo extremos. Además, colapsos y renacimientos de las poblaciones en un sistema de tres niveles se han observado en una versión extendida del modelo de Rabi cuántico, tanto en el régimen de acoplo ultrafuerte como en el profundo. Este trabajo abre la puerta para utilizar el sistema transmon-resonador en simulaciones o computaciones cuánticas, donde tales regímenes pueden mejorar las cualidades de los sistemas con las interacciones ya disponibles.

# Laburpena

Transmisio lerro multimododunetara akoplatutako transmoi qubitak deskribatzen dituen zirkuitu eredu bat proposatzen dugu. Eredu hau zirkuitu quantikoen elektrodinamikaren esparruan garatu da eta eskuragarri dauden datu esperimentalekin egiaztatu da, muturreko akoplo erregimenetan etorkizuneko esperimentuak diseinatzeko erabilgarria izan dadin. Hiru mailako sistemaren poblazioen kolapso eta berragerpenak behatu dira Rabiren eredu kuantikoaren hedapena diren akoplo ultraindartsuaren zein sakonaren erregimenetan. Lan honek ateak zabaltzen dizkio transmoi-erresonadore sistema simulazio zein konputazio kuantikoetan erabiltzeari, eta erregimenok berauetan dagoeneko eskuragarri dauden interakzio lanabesak hobetu ditzakete.

# *Acknowledgements*

Foremost, I would like to thank Prof. Enrique Solano for giving me the amazing opportunity of working in the QUTIS group, which is the closest I have ever been to the perfect (if it exists at all) scientific environment. Prof. Solano has had the ability to drive a group of very talented people in an extremely competitive business flowing many times in the opposite direction to the mainstream ideas. I thank him for teaching me the basic tools one needs not only to survive in such a world, but to outstand among the rest.

I want to thank Dr. Enrique Rico for his support during the whole year. Coming from an engineering background, I had to settle many basic ideas in physics and he has happily helped me to understand many of them. It has been a pleasure to work with him and I hope we can team up again in future projects. I want to thank Dr. Lucas Lamata for his overall help during the year, teaching us quantum optics and tipping me with very useful information.

I am also in debt to our collaborators at Delft University: Prof. Gary Steele, PhD. student Sal Bosman, and MSc. student Mario Gely, for amazing discussions and for kindly sharing spectrum data of their experiments, from which this thesis has benefited.

I would like to thank the members of the QUTIS "lunch team". In particular, Dr. Mikel Sanz, for being one of the more friendly and knowledgeable physicists I have ever worked with, Urtzi Las Heras, for having a toothpaste-ad smile everyday, except when sharing food and loosing in table tennis, Unai Álvarez for sharing with us his amazing music skills and being "just" such a nice guy (you have one more groupie in me), and Ryan Sweke, an amazing colleague and friend I have had the pleasure to meet in QUTIS.

I want to acknowledge also the TIME-office mates with Mr. Julen Pedernales at its front, for dealing with transfigurations abilities in everyday contexts, to Iñigo Arrazola for sharing his passion for physics in every group meeting and his mixed south american-basque artistic expertises and Ms. Xiao Hang with whom I shared, among other things, several steaks of truly unhealthy proportions.

I would also like to thank MSc.-"...very good grades in high school..." Laura García for being such an admirable person, a strong fighter and hopefully one day a good friend.

I want to thank my Masters colleagues Hodei Eneriz and Ander Tobalina for the good times shared through this crazy year, fighting side by side in every battle. I would also like to thank Mr. Miguel Ángel Simon for being such a good friend, physicist, musician and soon basketball player. It has been an honour to study, play, and talk with you.

I want to thank all my family, for being extremely supportive in the hard decisions I had to take in the last four years. I also want to thank them for teaching me the meaning of love and happiness and giving me an uncountable number of incredible opportunities. My parents and sister are my real heroes, and I feel extremely lucky to have grown with them. I want to specially thank Irene for weekly reminding me the meaning of life, and for sharing her great artistic skills. I want to thank all friends who are travelling with me through life, and in particular the one and only Prince of Persia Saeed Shojaee.

Last but not least, I want to thank Prof. Iñigo Luis Egusquiza, for having taught me so many physics and maths during this Masters, not only his lectures, but during multiple private

tutorials. That was an amazing exercise of generosity, which I will by no means forget. Together with Professors Manuel Ángel Valle and Juan Luis Mañes, you have given me the best treasure one can receive, knowledge. I also want to thank him for the fantastic time we had digging into the roots of the Sturm-Liouville problem, and of course, while playing basketball with the rest of his chaps.

# List of Figures

# Contents

# Chapter 1

# Introduction

Most of the greatest technological advances in the last century have been a consequence of the comprehension of quantum mechanics and the development of automatic computational machines. These two great achievements have preceded the growth of today's life quality and worldwide communication systems, and the improvement of working facilities. The development of quantum technologies in the last decades hopes to maintain the increase of computational resources at the same pace as Moore's law vaticinated back in 1965. Furthermore, extremely hard computational tasks like the factorization of big numbers [1] or the simulation of many body dynamics [2] are among the most prominent challenges the universal quantum computer [3] will be able to solve in the future. In contrast to classical computers, quantum computers take advantage of quantum phenomena like quantum superposition and entanglement to increase information storage and to provide a substantial speed up in the processing of units of information (qubits). In order to have such promising properties, quantum computers must keep big amounts of these building blocks in coherence; something that has not been achieved yet. Until the arrival of a flexibly programmable quantum computer, quantum simulators have been proposed as machines to tackle a smaller subset of very hard problems. These systems work by mapping the evolution of systems of interest into other systems where we have high control.

There have been many proposals for implementing both quantum computers and quantum simulators, readily trapped ions [4], quantum dots [5], NMR [6], ultracold atoms [7] and superconducting qubits [8, 9, 10, 11]. Each of them has proven to have its own strengths and drawbacks, but nevertheless, all of them share their excellent controllability of quantum systems like atoms, electrons and photons. Specifically, the efforts put in developing the trapped-ion technology were materialized in the 2012 Nobel Prize awarded to Serge Haroche and David Wineland, "for ground-breaking experimental methods that enable measuring and manipulation of individual quantum systems".

In the recent years, systems consisting of quantum circuits with superconducting qubits have overtaken all other technologies with the record of quantum information processing tasks [12]. The fundamental features of these circuits rely on the macroscopic quantum coherence that arises when microwave circuits are cooled down to temperatures on the order of miliKelvins. In that regime, most of the degrees of freedom get frozen, and the circuits become well described by collective and localized variables like voltages and currents, which obey the laws of quantum mechanics with properties such as quantum tunnelling, among others.

Superconducting circuits are solid state electrical circuits made out of linear elements like capacitors and inductors that can confine microwave photons, and non-linear elements like Josephson junctions that behave as artificial atoms. Coupling these elements together we can implement a perfect test-bed for cavity quantum electrodynamics. The ability to tailor their

frequencies and couplings at will endows superconducting qubits a great advantage over the rest of implementations; there is no "God-given" parameter that remains fixed. In particular, increasing the light-matter interaction to the so called ultrastrong coupling regime [14] and beyond [15] (strength of the coupling comparable or greater than the frequencies of the constituent elements) has only been achieved with quantum circuits. Reaching this barely explored regime does not only have fundamental interest (the idea of matter and light as individual subsystems breaks down), but it has also been proposed for performing quantum processing tasks faster [16] and for building quantum memories [17] in circuit QED [18].

In this thesis, we have focused on developing new models for describing superconducting qubits coupled to transmission line resonators (an element that holds a discrete number of microwave light modes), with the objective that this coupling reaches extreme regimes. In the first part, we investigate the possibility of reaching the ultrastrong coupling regime between a transmon qubit [19], the most successful superconducting qubit realisation, and the bosonic modes of a resonator. In the second part, we study typical features of the quantum Rabi model in the deep strong coupling regime [15], in an extended qutrit-like model of the anharmonic subsystem interacting with two bosonic modes.

More extensively, in chapter 2, we first introduce the basic models of cavity and circuit QED and the necessary theory of superconducting circuits that will be used throughout the thesis. We emphasise the quantum descriptions of transmission line resonators and the Cooper-pair box, precursor of the transmon qubit.

In chapter 3, we thoroughly analyse the possibility of coupling a transmon qubit to the bosonic modes of a resonator in the ultra strong regime. We first revise the original model of this system, and comment on the key parameters that could be engineered to increase the coupling. We propose next a new quantum model for transmission line resonators capacitively coupled to transmon qubits. Finally, we make use of experimental data provided by the group of Gary Steele at Delft University to probe this quantization procedure, and we comment on the possibility of using it as a new designing tool for future experiments.

In chapter 4, we anticipate possible features happening in a qutrit subsystem coupled to two modes of a resonator, where the frequencies of the three level system resemble those of a transmon qubit, and where the coupling parameters to the resonant mode are freely tuned. We briefly revise the perturbative ultrastrong coupling regime and the deep strong coupling regime before we analyse numerically our system, and evaluate the possibility of it being implemented with superconducting qubits.

In chapter 5, we conclude the discussion of the thesis explaining all the possible roads that this project opens. We make final remarks on the possibility of adding inhomogeneous transmission line resonators coupled to superconducting qubits to the quantum simulation toolbox.

# Chapter 2

# Circuit Quantum Electrodynamics

The field of quantum optics [20] studies the interaction between light and matter at its most fundamental level, by making use of the theory of quantum electrodynamics (QED) [21]. The size of matter typically considered in experimental quantum optics is that of atoms or molecules, although the theory of QED well describes the interplay between subatomic charged particles and photons. The main drawback from using atoms and photons is that their coupling in free space is very weak, and hence scattering events are very rare. In 1946 [22] it was discovered that putting atoms into cavities would enhance their fluorescence profile, giving birth to the field of cavity quantum electrodynamics (CQED) [23]. This area of research has become one of the most likely platforms for the practical implementation of quantum computation. There, units of information are typically encoded into the the discrete energy levels of atoms and data buses are mapped into flying photons. In this chapter, we are going to see the fundamental models of CQED and the basic tools one needs for implementing those in solid state circuits [11, 24], where atoms are replaced by artificial anharmonic systems and cavities are made of transmission line resonators.

## 2.1 Light-matter interactions: Jaynes-Cummings Model

The typical model of a simplified two level atom interacting with a single bosonic mode of a cavity resonator is the quantum Rabi Hamiltonian [25]

$$H_{Rabi} = \hbar\frac{\Omega_q}{2}\sigma_z + \hbar\omega_r\left(a^\dagger a + \frac{1}{2}\right) + \hbar g\sigma_x\left(a + a^\dagger\right) \tag{2.1}$$

where the first two terms account for a two-level subsystem or qubit with energy splitting $\Omega_q$ and operator $\sigma_z = (|e\rangle\langle e| - |g\rangle\langle g|)$ and a harmonic oscillator of frequency $\omega_r$ with creation and annihilation operators $a$ and $a^\dagger$ respectively. The third term of the Hamiltonian is the coupling between the qubit and the harmonic oscillator states written in the dipole approximation. This approximation states that when the size of the atom is much smaller than the wavelength of the cavity mode, the interaction can be written as $H_{int} = \hat{d}\cdot\hat{E}$ where $\hat{d} = d_{eg}\sigma_x$ is the dipole moment of the atom ($\sigma_x = (|e\rangle\langle g| + |g\rangle\langle e|)$ and $\hat{E}(x,t) = E_{rms}(a + a^\dagger)\sin kx$ is the quantized electric field in the cavity, where $E_{rms} = \sqrt{\hbar\omega_r/\epsilon_0 V}$ is the root mean square value of the electric field. The coupling constant can be then written as

$$g = \hbar^{-1} d_{eg} E_{rms} \sin kx. \tag{2.2}$$

If the coupling is small enough $g \ll \Omega_q, \omega_r$ the Rabi Hamiltonian (2.1) can be simplified by means of the rotating wave approximation (RWA), yielding the Jaynes-Cummings model [26]

$$H_{JC} = \hbar\frac{\Omega_q}{2}\sigma_z + \hbar\omega_r\left(a^\dagger a + \frac{1}{2}\right) + \hbar g\left(\sigma_+ a + \sigma_- a^\dagger\right). \tag{2.3}$$

This model has already been analytically solved and its diagonalization results in the eigenenergies

$$E_{g,0} = \hbar\frac{\Delta}{2}, \tag{2.4}$$

$$E_{\pm,n} = (n+1)\hbar\omega_r \pm \frac{\hbar}{2}\sqrt{4g^2(n+1)+\Delta^2}, \tag{2.5}$$

which are associated with the eigenstates $|g,0\rangle$ and

$$|+,n\rangle = \cos(\theta_n)|g,n+1\rangle + \sin(\theta_n)|e,n\rangle, \tag{2.6}$$

$$|-,n\rangle = -\sin(\theta_n)|g,n+1\rangle + \cos(\theta_n)|e,n\rangle, \tag{2.7}$$

where $\Delta = \Omega_q - \omega_r$ is the qubit-cavity detuning and $\theta_n$ is a mixing angle with the expression

$$\theta_n = \frac{1}{2}\arctan\left(\frac{2g\sqrt{n+1}}{\Delta}\right). \tag{2.8}$$

For the special situation where the qubit and the cavity are on resonance, i.e. $\Delta = 0$, the eigenstates of 2.3 simplify to

$$|\pm,n\rangle = \frac{1}{\sqrt{2}}\left(|g,n+1\rangle \pm |e,n\rangle\right). \tag{2.9}$$

The energy splitting with $n=0$, $\Delta E_{\pm,0} = 2g$ is also known as the vacuum Rabi splitting. If one lets an initial state with zero photons in the cavity and the atom excited $|\Psi(0)\rangle = |e,0\rangle$ evolve with the JC Hamiltonian $U = e^{iH_{JC}t/\hbar}$ the atom will coherently emit the photon into the cavity ($|g,1\rangle$) and then absorb it back with a frequency of $g/\pi$. Those oscillations are called Rabi oscillations, and in a closed system would last forever. However, real cavities and atoms lose energy irreversibly at rates $\gamma$ and $\kappa$ respectively and therefore Rabi oscillations can be seen in a time scale given by $\gamma+\kappa$. In order to see many Rabi oscillations, we require $g \gg \gamma, \kappa$, which is also known as the strong coupling regime. This coupling regime has proven to be very difficult to achieve with atoms/ions in cavities. A different approach was thus proposed to enhance the coupling; make use of "artificial" atoms (anharmonic systems with few computational states) built with superconducting circuits.

## 2.2 Circuit Quantum Electrodynamics

Originally, the implementation of cavity QED was conceived with real atoms interacting with optical photons. Nonetheless, such ideas can be realized can be made with any other physical system that can "hold" standing photons and make them interact with localized anharmonic (preferably two-level) systems. The implementation of cavity QED with microwave transmission lines and superconducting qubits fulfils these conditions, and this new research field is now known as circuit QED (cQED).

The greatest advantages to this mode of implementation are:

- All cQED Hamiltonian parameters can be engineered with great flexibility. In contrast, optical cavity QED relies on coupling and qubit frequencies which are set by nature.

- One can easily place many qubits in a transmission line resonator to make them all interact with the same bosonic modes. Although in principle this is also possible in cavity QED, the extreme difficulty of such experiments has delayed its implementation.
- Qubit and coupling parameters can be not only predesigned at will, but they are also highly tunable during an experiment.
- Light-matter interaction beyond the strong coupling regime has only been reported in cQED systems, i.e. the ultrastrong coupling regime [27, 14]. Until now, no physical limit for the coupling has been discovered.

On the other hand, their design flexibility carries an important drawback; loss of coherence between the qubits and the photons is also greater than in atomic systems. Nevertheless, its fast interactions have allowed us to produce experiments unachievable with any other implementation. We will now present the basic tools necessary to describe circuit QED systems.

### 2.2.1 Lumped-element circuit quantization

Electric circuits obey Maxwell's equations when they work in their classical regime, i.e. when the number of particles is macroscopic and the temperature is high enough for individual scattering processes between constituents to effectively behave as a background noise. Amazingly, when they are cooled down to temperatures very close to absolute zero macroscopic quantum phenomena emerge, in other words, collective degrees of freedom of the circuit (like voltages or currents) evolve under the Schrödinger equation. The standard procedure to describe the quantum behaviour of electric circuits consists in finding the classical Hamiltonian dynamics of an effective network model, and imposing canonical commutation relations on its degrees of freedom. We will summarize the general formalism introduced in [28, 29] to find quantum circuit Hamiltonians that will be used throughout this thesis, restricting ourselves to circuits containing passive non-dissipative elements, i.e. we will not take into consideration impedances resulting in energy decay in the system.

An electric circuit is typically modelled as a network of two-terminal components connected in nodes, which in a specific regime of parameters behave under Kirchhoff voltage and current laws [30], see Fig. 2.1. We can identify the nodes of the network with a potential set of degrees of freedom of the circuit (symmetries in the system can effectively reduce this number). The usual degrees of freedom used in classical electrical engineering are the voltages $V(t)$ in the nodes and the currents $I(t)$ in the loops, but for quantum circuits we will use the equivalent node fluxes $\Phi(t)$ and loop charges $Q(t)$, which are related to the previous ones via

$$\Phi(t) = \int_{-\infty}^{t} V(t')dt', \; Q(t) = \int_{-\infty}^{t} I(t')dt'. \tag{2.10}$$

This choice of variables is much more appropriate for superconducting circuits because flux and charge variables are very closely related to the superconducting phase across a Josephson junction, as well as the difference in the number of Cooper pairs, as we will see later in Sec. 2.3. If we apply Kirchhoff's laws at the nodes of the network we can find the equations of motion for the flux variables $\{\Phi_k(t)\}_{k=1,...,n}$, which in classical mechanics are regarded as the Euler-Lagrange equations

$$\frac{d}{dt}\left(\frac{\partial L}{\partial \dot{\Phi}_k}\right) - \frac{\partial L}{\partial \Phi_k} = 0, \; k = 1, ..., n \tag{2.11}$$

associated to a Lagrangian family (infinitely many Lagrangians will have the same equations of motion). We remark here that choosing the flux variables for writing the Lagrangian is mostly

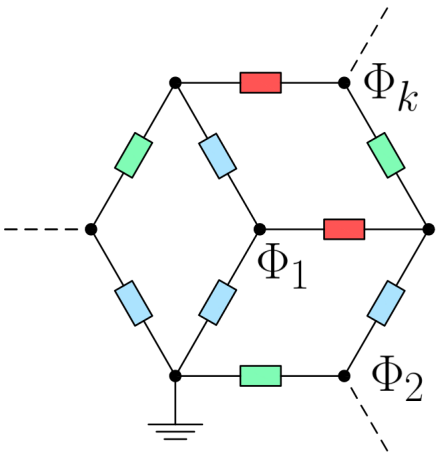


Figure 2.1: General network of lumped elements. Flux nodes $\{\Phi_k\}_{k=1,...,n}$ define a set of dynamical variables with $n$ being an upper bound to the number of degrees of freedom of the classical system.

used as the non-linear element that successful superconducting qubits have are the Josephson junctions. However, a completely equivalent description starting with the loop charges can be equally useful when describing circuits with phase-slip junctions, a non-linear element in charge variable, see [31]. If we consider for the moment the only two non-dissipative linear elements that exist in circuits, capacitors and inductances, any found Lagrangian that accomplishes (2.11) is just the difference between the electric and magnetic energy stored in those elements respectively

$$L(\Phi_k, \dot{\Phi}_k) = \frac{1}{2}\dot{\vec{\Phi}}^T C \dot{\vec{\Phi}} - \frac{1}{2}\vec{\Phi}^T L \vec{\Phi}, \tag{2.12}$$

where $C$, $L$ are the capacitance and inductance matrix of the circuit and $\vec{\Phi} = (\Phi_1, \Phi_2, ...)$. The associated classical Hamiltonian can be obtained by applying the Legendre transformation

$$H(\Phi_k, Q_k) = \sum_k Q_k \dot{\Phi}_k - L, \tag{2.13}$$

where the charges $Q_k$ are the conjugate variables to the fluxes $\Phi_k$ satisfying the Poisson bracket $\{\Phi_k, Q_k\} = \delta_{k,k'}$. The final step is then to apply the canonical quantization procedure to the classical degrees of freedom $\left[\hat{\Phi}_k, \hat{Q}_k\right] = i\hbar$, yielding the quantum Hamiltonian description of the circuit,

$$\hat{H} = \frac{1}{2}\vec{\hat{Q}}^T C \vec{\hat{Q}} + \frac{1}{2}\vec{\hat{\Phi}}^T L \vec{\hat{\Phi}}. \tag{2.14}$$

We will apply this formalism for the quantization of circuits that will collectively operate as cavity QED systems.

### 2.2.2 Transmission lines

As optical cavities confine the electromagnetic field in the terahertz frequency range, transmission line resonators play the same role for photons that are in the microwave regime. Thus,

we review now the quantization procedure for describing these important components in circuit QED systems.

In microwave engineering [30], transmission line theory makes use of lumped element circuits to study the propagation of waves in environments enclosed by conductors. In Fig. 2.2, we see a schematic representation of the lossless transmission line as a two-wired line with characteristic impedance $Z_0 \equiv \sqrt{L/C}$ and propagation constant $\beta \equiv \omega\sqrt{LC}$, and its associated lumped element circuit model of a $\Delta x$ length of the line where $L(C)$ is the inductance (capacitance) per unit of length. In order to study the quantum behaviour of transmission line elements we can

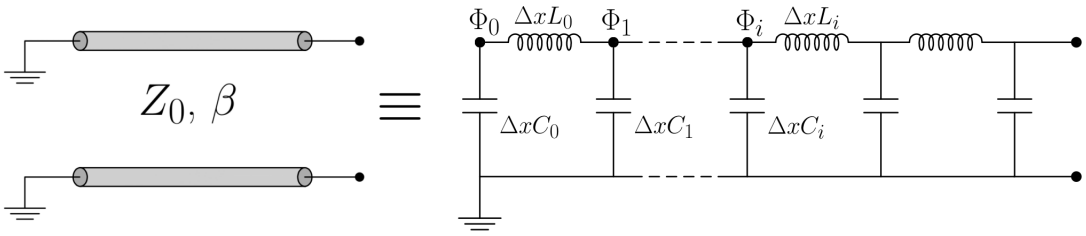


Figure 2.2: Schematic representation of a transmission line resonator by a two-wired line that supports a TEM mode with characteristic impedance $Z_0$ and propagation constant $\beta$, and its equivalent lumped element circuit model, where $L_i(C_i)$ is the inductance (capacitance) per unit of length $\Delta x$ and $\Phi_i$ the flux variable at each node.

get the classical Lagrangian of the lumped element model in terms of its normal modes. We will then write its associated Hamiltonian, and make use of the canonical quantization procedure [28, 29]. Using nodal analysis we can then easily write a Lagrangian for the circuit of Fig. 2.2(b),

$$L = \sum_i \Delta x \, \frac{C_i}{2} \dot{\Phi}_i(t)^2 - \frac{1}{2\Delta x \, L_i} \left(\Phi_i(t) - \Phi_{i+1}(t)\right)^2 \tag{2.15}$$

which in the continuum limit of $\Delta x \to 0$ and $\sum_i \Delta x \to \int_a^b dx$ transforms into

$$L = \frac{1}{2} \int_a^b dx \left( C(x) \left(\partial_t \Phi(x,t)\right)^2 - \frac{1}{L(x)} \left(\partial_x \Phi(x,t)\right)^2 \right) \tag{2.16}$$

where $C_i \to C(x_i)$, $L_i \to L(x_i)$, $\left(\Phi_i(t) - \Phi_{i+1}(t)\right)/\Delta x \to \partial_x \Phi(x_i, t)$, $\Phi_i(t) \to \Phi(x_i, t)$. We will now see how the action

$$S = \int_0^T dt L = \frac{1}{2} \int_0^T dt \int_a^b dx \left( C(x) \left(\partial_t \Phi(x,t)\right)^2 - \frac{1}{L(x)} \left(\partial_x \Phi(x,t)\right)^2 \right) \tag{2.17}$$

associated with that Lagrangian already implies boundary conditions to the fields $\Phi(x,t)$. We make use of the principle of least action and take the variation of the action $\delta S$ such that

$$
\begin{aligned}
\delta S &= \int_0^T dt \delta L \\
&= \int_0^T dt \int_a^b dx \left( \frac{C(x)}{2} \partial_t \Phi(x,t)\, \delta(\partial_t \Phi(x,t)) - \frac{1}{2L(x)} \partial_x \Phi(x,t)\, \delta(\partial_x \Phi(x,t)) \right) \\
&= \int_0^T dt \int_a^b dx \left( \frac{C(x)}{2} \partial_t \Phi(x,t)\, \partial_t(\delta \Phi(x,t)) - \frac{1}{2L(x)} \partial_x \Phi(x,t)\, \partial_x(\delta \Phi(x,t)) \right) \\
&= \int_a^b dx\, C(x) \left( [\partial_t \Phi(x,t)\, \delta \Phi(x,t)]_0^T - \int_0^T dt\, \partial_{tt} \Phi(x,t)\, \delta \Phi(x,t) \right) \\
&- \int_0^T dt \left( \left[ \frac{\partial_x \Phi(x,t)}{L(x)} \delta \Phi(x,t) \right]_a^b - \int_a^b dx\, \partial_x \left( \frac{\partial_x \Phi(x,t)}{L(x)} \right) \delta \Phi(x,t) \right) = 0, \qquad (2.18)
\end{aligned}
$$

where to go from the third to fifth line we have integrated by parts with respect to time (space) the kinetic (potential) term associated with the capacitance (inductance). In Eq. (2.18), we have two types of boundary terms, temporal and spatial. We further recall that implementing the principle of least action requires to set the variation of the fields at the initial and final time to zero $\delta\Phi(x,0) = \delta\Phi(x,T) = 0$. We are thus left with just the spatial boundary term, namely (up to a sign and a factor 2)

$$\int_0^T \left[ \frac{1}{L} \Phi' \delta \Phi \right]_a^b$$

which can be set to zero in different ways: a first one is to impose that the variations be zero at the spatial boundary,

$$\delta\Phi(a,t) = \delta\Phi(b,t) = 0, \qquad (2.19)$$

which for the transmission line problem means leaving the end terminals unconnected. Another one is to impose the vanishing of the spatial derivatives at the boundary, $\delta\Phi'(a,t) = \delta\Phi'(b,t) = 0$. Inserting the first set of spatial boundary conditions on Eq. (2.18) we can get the final equations:

$$C(x)\, \partial_{tt}(\Phi(x,t)) - \partial_x \left( \frac{\partial_x \Phi(x,t)}{L(x)} \right) = 0 \qquad (2.20)$$

$$\frac{\partial_x \Phi(a,t)}{L(x)} = f_a(t), \quad \frac{\partial_x \Phi(b,t)}{L(x)} = f_b(t), \qquad (2.21)$$

where the functions $f_a(t)$ and $f_b(t)$ are not degrees of freedom but fixed arbitrary time dependent functions.

**Normal modes of homogeneous transmission line:**

A transmission line of finite length $l$ grounded at $x = 0$ and terminated in open circuit at $x = l$ with constant capacitance ($C_0$) and inductance ($L_0$) per unit length has the equations

$$\ddot{\Phi}(x,t)) - \frac{1}{C_0 L_0} \Phi''(x,t) = 0 \qquad (2.22)$$

$$\Phi(0,t) = \Phi'(l,t) = 0, \qquad (2.23)$$

where we have denoted the partial spatial (time) derivative as $\Phi'(x,t)$ ($\dot{\Phi}(x,t)$). It must also be remarked, that in deriving (2.23), we have used a mixed case of spatial boundaries $\delta\Phi'(0,t) =$

$\delta\Phi(l,t) = 0$. The above set of equations corresponds to a discrete multimode resonator. We can write the Lagrangian in the normal mode basis by expanding the field in a complete set of eigenfunctions $\{u_n(x)\}$

$$\Phi(x,t) = \sum_n \psi_n(t)\, u_n(x). \tag{2.24}$$

Substituting in (2.22)-(2.23) we derive the equations

$$\frac{\ddot{\psi}_n(t)}{\psi_n(t)} = -\omega_n^2, \tag{2.25}$$

$$\frac{u_n''(x)}{L_0} = -\omega_n^2 C_0 u_n(x), \tag{2.26}$$

$$u_n(0) = 0, \tag{2.27}$$

$$u_n'(l) = 0, \tag{2.28}$$

corresponding to a Sturm-Liouville problem. Eqs. (2.25)-(2.27) admit the solution $u_n(x) = A_n \sin(k_n x)$, and inserting this ansatz into (2.28) we are able to derive the equation for the wave numbers

$$k_n = (2n+1)\frac{\pi}{2l}.$$

The complete set of eigenfunctions$\{u_n(x)\}$ form a basis with the orthogonality condition

$$\frac{2}{A_n^2}\int_0^l dx\, C_0 u_n(x) u_m(x) = C_r \delta_{nm}, \tag{2.29}$$

where $C_r = \int_0^l C_0 dx = C_0 l$. We can write now the Lagrangian (2.16) with the sum of eigenmodes and the orthogonality relation to get

$$L = \sum_n \frac{C_r}{2}\left(\dot{\psi}_n^2 - \omega_n^2 \psi_n^2\right). \tag{2.30}$$

We define the conjugate momenta to the fluxes $\psi_n$, the charges $q_n = C_r \dot{\psi}_n$ and do a change of variables of fluxes and charges in terms of creation and annihilation operators

$$\psi_n = \sqrt{\frac{\hbar}{2\omega_n C_r}}\left(a_n^\dagger + a_n\right), \tag{2.31}$$

$$q_n = i\sqrt{\frac{\hbar\omega_n C_r}{2}}\left(a_n^\dagger - a_n\right), \tag{2.32}$$

with $a_n$ and $a_n^\dagger$ satisfying the commutation relation $\left[a_n, a_m^\dagger\right] = \delta_{nm}$ such that the final quantum Hamiltonian reads

$$\hat{H} = \sum_n \omega_n \left(a_n^\dagger a_n + \frac{1}{2}\right). \tag{2.33}$$

Thus, we have showed that the homogeneous quantized transmission line resonator can be also seen as an infinite sum of a discrete set of harmonic oscillators equally spaced.

## 2.3 Superconducting Qubits

Superconducting qubits are circuits made of Josephson junctions which behave as two level systems. Due to their very flexible design they have been called "artificial" atoms. In the last twenty years they have overtaken all of the other qubit implementation proposals and have allowed for implementation of the most complex quantum algorithms yet [32, 12]. In this section we are going to briefly review the fundamentals of this technology introducing the Josephson junction, i.e. the non-linear non-dissipative element that all qubits share, and the Cooper-pair Box qubit which laid the foundation for the very succesful transmon qubit [19] that we will thoroughly study in Chapter 3.

### 2.3.1 Josephson effect and Josephson junction

A Josephson junction is made of two superconductors separated by a thin insulating layer, see Fig. 2.3(a). The two superconductors can be effectively characterized by a macroscopic wave function $\Psi_i = \sqrt{n_i}e^{i\varphi_i}$ [33]. Brian Josephson [34] showed that these two wave functions can overlap with each other, with the net result of tunnelling processes of Cooper-pairs (pairs of electrons) between the two superconductors. The solution of the Schrödinger equation of that system demonstrates that the flowing current through the junction can be written in terms of the phase difference of the wave functions via

$$I_J = I_c \sin(\varphi_2 - \varphi_1) = I_c \sin\varphi_J, \tag{2.34}$$

where $I_c$ is the critical current of the junction (which depends among other things on microscopic features like the area and thickness of the junction) and $\varphi_J$ is the so-called gauge invariant phase. This relation is also known as the dc-Josephson relation because in the absence of any externally applied voltage bias $V$ there is a continuous flow of dc-current. There is a second fundamental equation known as the ac-Josephson relation which relates a non-zero applied voltage V between the two superconductors with the gauge invariant phase $\varphi_J$ via

$$V = \frac{\Phi_0}{2\pi}\frac{d\varphi_J}{dt}, \tag{2.35}$$

where $\Phi_0 = 2e/\hbar$ is the magnetic flux quantum, whose name comes from the fact that a magnetic flux passing through a superconducting ring is quantized in units of $\Phi_0$ [33]. Eq. (2.34) can be plugged into (2.35) yielding the non-linear oscillating current in the junction $I = I_c \sin(2\pi V t/\Phi_0)$. Using the usual inductance definition $L = V/\dot{I}$, we can derive the associated non linear inductance of the Josephson junction,

$$L_J = \frac{\Phi_0}{2I_c\cos(\varphi_J)}. \tag{2.36}$$

There is an equivalent circuit model of the Josephson junction consisting in a pure non-linear inductance and a capacitor shunting it, see Fig. 2.3(b). By means of the relation between flux and voltage $V = d\Phi/dt$ and the ac-Josephson relation (2.35) we can write explicitly the relation between the flux and phase across the junction

$$\varphi_J = 2\pi\Phi_J/\Phi_0. \tag{2.37}$$

We can finally derive the Hamiltonian of a Josephson junction applying the Kirchhoff equation to the circuit in Fig. 2.35(b), containing the equation $C_J\ddot{\Phi}_J = I_c\sin(2\pi\Phi_J/\Phi_0)$ where $\Phi_J = \Phi_2 - \Phi_1$ corresponding to the Lagrangian

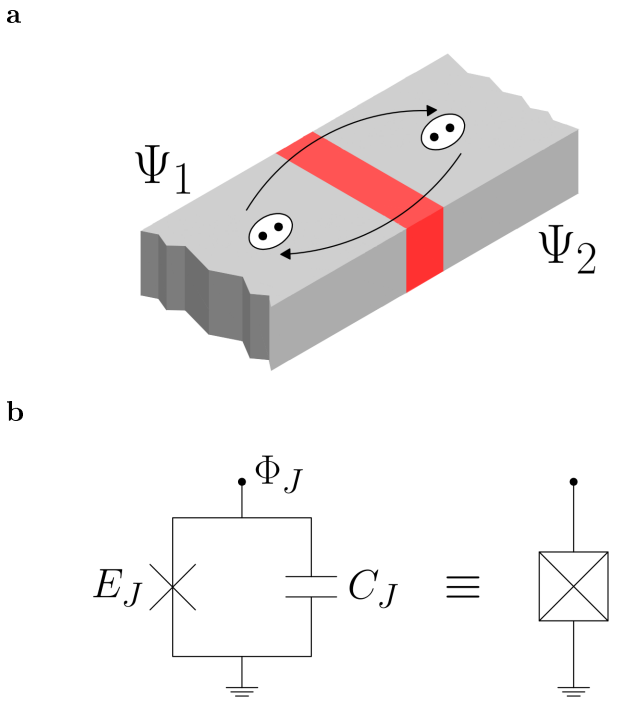


Figure 2.3: (**a**) Josephson junction with superconducting wave functions $\Psi_{1,2}$ and (**b**) a circuit schematic of junction formed by a non-linear inductive term $E_J$ shunted by a capacitor $C_J$ with its usual box representation.

$$L = \frac{C_J}{2}\dot{\Phi}_J^2 - \frac{I_c\Phi_0}{2\pi}\left[1 - \cos\left(\frac{2\pi\Phi_J}{\Phi_0}\right)\right]. \tag{2.38}$$

Performing the Legendre transformation, we finally derive the Hamiltonian

$$\begin{aligned} H_J &= \frac{\hat{Q}_J^2}{2C_J} - \frac{I_c\Phi_0}{2\pi}\cos\left(\frac{2\pi\hat{\Phi}_J}{\Phi_0}\right) \\ &= 4E_C\hat{n}^2 - E_J\cos\left(\hat{\varphi}_J\right) \end{aligned} \tag{2.39}$$

where we have expressed the charge in terms of the difference number of Cooper pairs in the two superconductors $\hat{Q} = 2e\hat{n}$. We also define the charge energy $E_C \equiv e^2/2C_J$ and the Josephson energy $E_J = I_c\Phi_0/2\pi$. This non-linear cosine potential is the key to construct systems whose energy spectra is reduced to two-level systems (qubits). The above Hamiltonian can be written in the Cooper-pair number basis $|n\rangle$ which satisfies $\hat{n}|n\rangle = n|n\rangle$ by introducing the relation between phase $|\varphi\rangle$ and number basis

$$|n\rangle = \frac{1}{2\pi}\int_0^{2\pi} d\varphi' e^{in\varphi'}|\varphi'\rangle. \tag{2.40}$$

We can now write the operator $e^{i\hat{\varphi}}$ in the $|n\rangle$ basis by checking how it acts on number states $|n\rangle$

$$
\begin{aligned}
e^{i\hat{\varphi}}|n\rangle &= \frac{1}{2\pi}\int_0^{2\pi} d\varphi' e^{i\varphi'}|\varphi'\rangle\langle\varphi'|n\rangle \\
&= \frac{1}{2\pi}\int_0^{2\pi} d\varphi' e^{i(n+1)\varphi'}|\varphi'\rangle \\
&= |n+1\rangle. \qquad (2.41)
\end{aligned}
$$

As the above is valid for all states $|n\rangle$, we then have that $e^{i\hat{\varphi}} = \sum_n |n+1\rangle\langle n|$ and therefore

$$H = 4E_C \sum_n n^2 |n\rangle\langle n| - \frac{E_J}{2}\left(\sum_n |n+1\rangle\langle n| + \sum_n |n\rangle\langle n+1|\right). \qquad (2.42)$$

It can be checked that the Cooper-pair number $\hat{n}$ and phase $\hat{\varphi}$ operators are conjugate variables that satisfy $[\hat{\varphi}, \hat{n}] = i$. We are going to see now a simple variation of the above circuit which was used as the first superconducting qubit.

### 2.3.2 Cooper-pair Box

The Cooper Pair Box [35, 36] is the origin of all charge qubits. It consists of a small superconducting island in between a Josephson junction and a capacitor plate that is biased by a voltage source, see Fig. 2.4. The Hamiltonian of this circuit can be calculated with the same procedure of Subsec. 2.2.1 but we will leave its derivation for the related circuit of the transmon qubit in Sec. 3.1.1. The Hamiltonian description then obtained is

$$H_{CPB} = 4E_C(\hat{n} - n_g)^2 - E_J \cos(\hat{\varphi}_J), \qquad (2.43)$$

where the charge energy is defined as $E_C = e^2/2\,(C_g + C_J)$, and the charge offset as $n_g = C_g V_g/2$. We calculate the energy spectrum of the CPB Hamiltonian using the Matrix Numerov

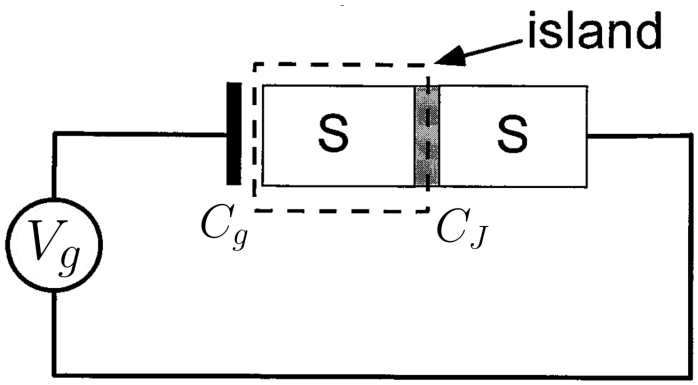


Figure 2.4: Cooper Pair Box schematic circuit: two superconducting plates form the Josephson junction with energy $E_J$ and capacitance $C_J$. The gate capacitance $C_g$ couples the junction to a voltage source $V_g$ to bias the number of Cooper pairs in the island. Figure taken from [36] and modified.

Method [37]. The Schrödinger equation in the phase space

$$H_{CPB}\Psi(\varphi) = \left[4E_C(-i\frac{d}{d\varphi} + n_g)^2 - E_J\cos(\varphi)\right]\Psi(\varphi) = E\Psi(\varphi), \qquad (2.44)$$

has the boundary condition $\Psi(\varphi) = \Psi(\varphi + 2\pi)$. We can eliminate the charge offset by performing the gauge transformation $\Psi'(\varphi) = e^{-2in_g\varphi}\Psi(\varphi)$,

$$\left[-4E_C\frac{d^2}{d\varphi^2} - E_J\,\cos(\varphi)\right]\Psi'(\varphi) = E\Psi'(\varphi)\,, \tag{2.45}$$

with the new boundary condition $\Psi'(\varphi) = e^{-2in_g\pi}\Psi'(\varphi + 2\pi)$. For the general differential equation $\psi''(x) = f(x)\,\psi(x)$, the standard Numerov method [38] has the stepwise integration formula

$$\psi_{i+1} = \frac{\psi_{i-1}\left(12 - d^2 f_{i-1}\right) - 2\psi_i\left(5d^2 f_i + 12\right)}{d^2 f_{i+1} - 12} + O(d^6), \tag{2.46}$$

with $\Psi_i = \Psi(x_i)$, $f_i = f(x_i)$, $i \in \{1, ..., N\}$ and $d$ being the bin size in the discretization where in our case $f(x) = -(E - V(x))/4E_C$ and $V(x) = -E_J\,\cos(x)$. Eq. (2.46) can be rearranged into matrix form as

$$-4E_C A\psi + BV\psi = EB\psi, \tag{2.47}$$

where we have defined $\psi = (..., \psi_i, \psi_{i+1}, ...)$, $A = (\mathbb{1}_{-1} - 2\mathbb{1}_0 + \mathbb{1}_1)/d^2$, $B = (\mathbb{1}_{-1} + 10\mathbb{1}_0 + \mathbb{1}_1)/12$, $V = \mathrm{diag}(..., V_i, V_{i+1}, ...)$ and $I_p$ is the matrix with 1s along its $p$th diagonal and zeros elsewhere. Multiplying by $B^{-1}$, we obtain

$$-4E_C B^{-1} A\psi + V\psi = E\psi. \tag{2.48}$$

We finish the discretization of Eq. (2.45) by adding the boundary condition for our periodic potential after the gauge transformation $A_{1,N} = A_{N,1} = e^{-2in_g\pi}/d^2$ and $B_{1,N} = B_{N,1} = e^{-2in_g\pi}/12$. The numerical diagonalization of Eq. (2.45) is shown in Fig. 2.5. It can be noted that it faithfully reproduces the perfect Mathieu solution in Fig. 2 of [19] for different ratios of $E_J/E_C$. In the CPB regime ($E_C \geq E_J$, see Fig. 2.5(a)) the eigenstates are very anharmonic but they strongly depend on the offset charge, which means that the charge noise channel will be very important. On the other hand, the so called transmon regime corresponds to $E_J > E_C$ and is much more resilient to charge noise fluctuations, see Sec. V in [19]. In both cases, the difference of energy between the first and second transitions is big enough to be able to address the two-level subsystem, and remain there enough time to perform quantum operations.

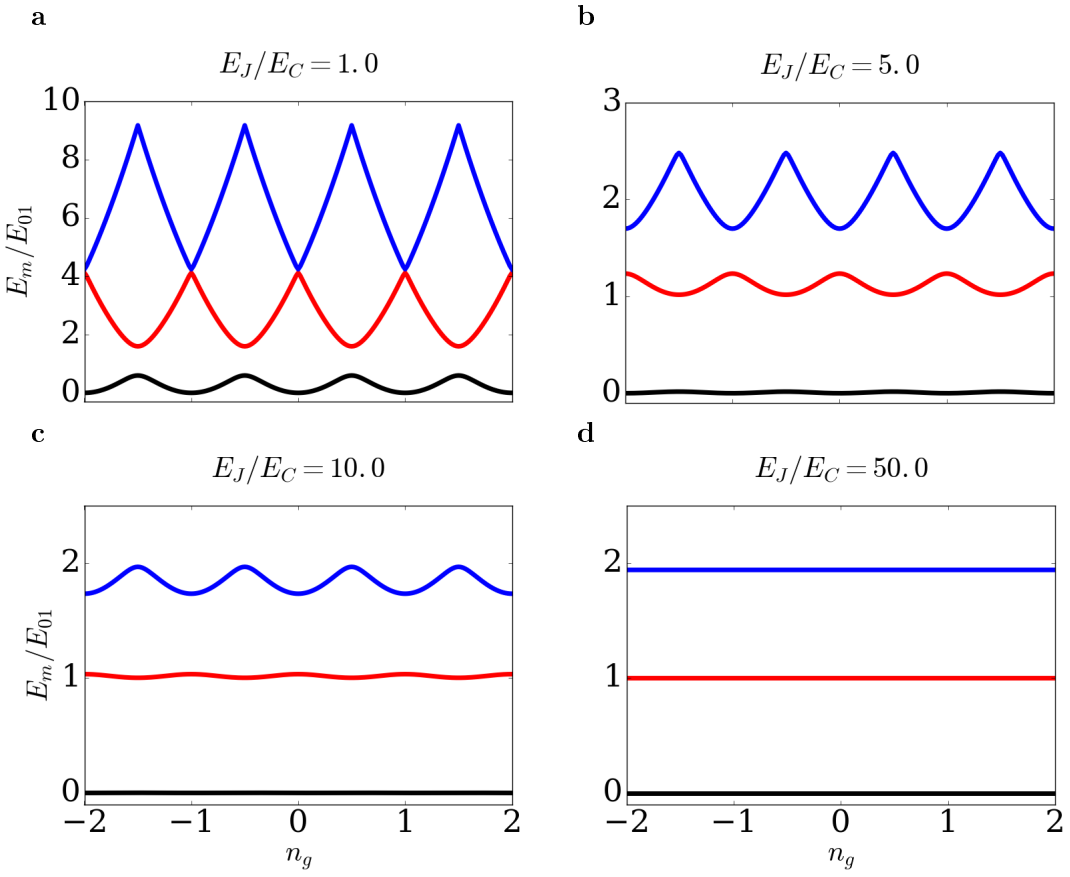


Figure 2.5: Energy levels of the CPB as a function of the charge offset $n_g$ using the Matrix Numerov Method for different values of $E_J/E_C$. As this ratio increases the levels of the CPB become more harmonic and more resilient to charge bias noise. For $E_J/E_C \gg 1$ the system is known as transmon qubit.

# Chapter 3

# Circuit QED with a transmon qubit in the USC regime

The transmon [19] has been one of the most successful qubits in the field of cQED. Among its best features are some of the lowest decay and decoherence rates of all superconducting qubits. Furthermore, its coupling to transmission line buses can be increased faster than its simultaneous loss of anharmonicity and, when used in 3D cavities transmon qubits can exhibit even more robustness against noise [39]. In the community of quantum optics, there is a great interest in having systems working in regimes where the rotating wave approximation fails, which would allow to study new states of matter [27, 13]. Likewise, there have been proposals to use such tools to do quantum information processing tasks, e.g. ultra fast quantum gates [16]. However, as of yet, nobody has performed an experiment with a transmon qubit ultrastrongly coupled to a resonator. The difficulty of the task has been theoretically discussed [14], but no important progress has been made up to now. In this section we are going to present a theoretical model of a transmission line resonator capacitively coupled to a transmon qubit, where the ultrastrong coupling regime between a mode of the resonator and the transmon could be engineered. We will test the model with data from a new experiment that has been performed in the laboratory of Pr. Gary Steele at Delft University of Technology. We will show that in this experimental realisation the USC non-resonant coupling regime has been achieved. However, first we will review the original transmon qubit proposal by Koch et al. [19], paying special attention to the critical parameter values required to reach that goal.

## 3.1 Transmon qubit revisited

The transmon qubit was originally realised with a Cooper-Pair Box embedded in a transmission line resonator, with Josephson energy $E_J \gg E_C$. A schematic diagram and an effective circuit model of the circuit can be seen in Fig. 3.1. Two Josephson junctions are threaded by a magnetic flux, such that they behave like an effective junction with tunable Josephson energy $E_J = E_{J,max} \left|\cos(\pi\Phi_{ext}/\Phi_0)\right|$ (a dc-SQUID). In this first section we are going to assume that the Josephson junctions are identical and we will leave the asymmetric case for later study in Sec. 3.1.3. This effective Josephson junction is capacitively coupled through $C_g$ to a resonator, simply modelled as a LC-resonator (first mode of the transmission line resonator). The effective offset charge $n_g$ (number of Cooper pairs) is controlled by a constant voltage source $V_g$ in a similar manner to the CPB, see Sec. 2.3.2. The main difference of the transmon as compared with the common CPB, is the shunting of the Josephson junctions with a huge capacitor $C_B$, together with an increase of the capacitance $C_g$.

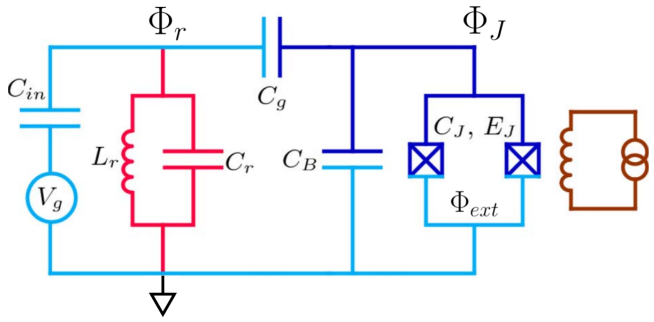


Figure 3.1: Effective circuit diagram of the transmon qubit (two Josephson junctions in parallel) coupled through capacitance $C_g$ to the resonator with inductance $L_r$ and capacitance $C_r$ and biased by the voltage source $V_g$. Figure taken from [19] and slightly modified.

### 3.1.1 Circuit quantization

In order to model the quantum behaviour of this circuit we will follow [29] to derive a Hamiltonian. Again, we start by writing the Lagrangian of the circuit which can be directly done from the node description of Fig. 3.1(b)

$$L = \frac{1}{2}C_{in}\left(\dot{\Phi}_r - V_g\right)^2 - \frac{1}{2L_r}\Phi_r^2 + \frac{1}{2}C_r\dot{\Phi}_r^2 + \frac{C_g}{2}\left(\dot{\Phi}_J - \dot{\Phi}_r\right)^2 + \frac{C_A}{2}\dot{\Phi}_J^2 + E_J\cos\left(\varphi_J\right), \tag{3.1}$$

where $\Phi_{r,J}$ are the node fluxes that define the resonator and the Josephson degrees of freedom respectively, the Josephson phase is $\varphi_J \equiv 2\pi\Phi_J/\Phi_0$ and $C_{in}$ is the capacitance between the voltage bias $V_g$ and the resonator and $C_A = C_B + C_J$. We define the conjugate coordinates to the node fluxes, the associated charges

$$Q_r \equiv \frac{\partial\mathcal{L}}{\partial\dot{\Phi}_r} = C_r\dot{\Phi}_r - C_g\left(\dot{\Phi}_J - \dot{\Phi}_r\right) + C_{in}\left(\dot{\Phi}_J - V_g\right), \tag{3.2}$$

$$Q_J \equiv \frac{\partial\mathcal{L}}{\partial\dot{\Phi}_J} = C_r\dot{\Phi}_r + C_g\left(\dot{\Phi}_J - \dot{\Phi}_r\right) + C_A\dot{\Phi}_J, \tag{3.3}$$

with inverse relations

$$\dot{\Phi}_r = Q_r\frac{(C_A + C_g)}{C_*^2} + Q_J\frac{C_g}{C_*^2} + V_g\frac{C_{in}\left(C_A + C_g\right)}{C_*^2}, \tag{3.4}$$

$$\dot{\Phi}_J = Q_r\frac{C_g}{C_*^2} + \frac{Q_J}{C_A + C_g}\left(1 + \frac{C_g^2}{C_*^2}\right) + V_g\frac{C_{in}C_g}{C_*^2}, \tag{3.5}$$

where $C_*^2 \equiv C_g(C_{in} + C_r) + C_A(C_g + C_{in} + C_r)$. We perform a Legendre transformation and promote the conjugate variables to operators, with commutation relations $\left[\hat{\Phi}_i, \hat{Q}_j\right] = i\hbar\delta_{ij}$, and obtain the quantum Hamiltonian

$$\begin{aligned} H = \; & \frac{(C_A + C_g)}{2C_*^2}\hat{Q}_r^2 + \frac{1}{2L_r}\hat{\Phi}_r^2 + \frac{(C_g + C_{in} + C_r)}{2C_*^2}\hat{Q}_J^2 - E_J\cos\left(\hat{\varphi}_J\right) \\ & + \frac{C_g}{C_*^2}\hat{Q}_J\hat{Q}_r + \frac{\left(C_A + C_g\right)C_{in}}{C_*^2}\hat{Q}_r V_g + \frac{C_g C_{in}}{C_*^2}\hat{Q}_J V_g. \end{aligned} \tag{3.6}$$

If one engineers the capacitances such that $C_r \gg C_A$, $C_{in}$, $C_g$ and define the total capacitance $C_\Sigma \equiv C_A + C_g$, we arrive at

$$\begin{aligned} H \simeq \; & \frac{\hat{Q}_r^2}{2C_r} + \frac{1}{2L_r}\hat{\Phi}_r^2 + \frac{\hat{Q}_J^2}{2C_\Sigma} - E_J \cos\left(\hat{\varphi}_J\right) \\ & + \frac{C_g}{C_r C_\Sigma}\hat{Q}_J\hat{Q}_r + \frac{C_{in}}{C_r}\hat{Q}_r V_g + \frac{C_g C_{in}}{C_r C_\Sigma}\hat{Q}_J V_g. \end{aligned} \tag{3.7}$$

We now introduce (i) creation and annihilation operators

$$\hat{a}^\dagger,\, \hat{a} \equiv \frac{1}{\sqrt{2\hbar}}\left(\left(\frac{C_r}{L_r}\right)^{1/4}\hat{\Phi}_i \mp i\left(\frac{L_r}{C_r}\right)\hat{Q}_i\right) \tag{3.8}$$

of quanta of energy in the LC-oscillator of frequency $\omega_r = 1/\sqrt{L_r C_r}$ and (ii) its root-mean-square voltage $V_{rms}^0 = \sqrt{\hbar\omega_r/2C_r}$. We also define the ratio $\beta \equiv C_g/C_\Sigma$ between the gate capacitance and total capacitance, as well as the charge energy $E_C = e^2/2C_\Sigma$, in order to put the Hamiltonian into the circuit QED form of Eq. (3.1) in [19],

$$H = 4E_C(\hat{n} - n_g)^2 - E_J\cos(\hat{\varphi}_J) + \hbar\omega_r\hat{a}^\dagger\hat{a} + 2\beta e V_{rms}^0\hat{n}\left(\hat{a} + \hat{a}^\dagger\right), \tag{3.9}$$

where the effective offset gauge charge is defined as $n_g = -C_g C_{in} V_g/2C_r e$. In the above derivation we have neglected the constant term $n_g^2$ and the coupling term between the resonator charge $\hat{Q}_r$ and $V_g$, which could be used to drive the resonator mode with an oscillatory source.

### 3.1.2 Circuit QED with the transmon in the USC regime

Recalling the diagonalization of the qubit subsystem done in Sec. 2.3.2, we can rewrite Eq. (3.9) in the generalised Rabi Hamiltonian form

$$H = \hbar\sum_i \Omega_i \left|i\right\rangle\left\langle i\right| + \hbar\omega_r\hat{a}^\dagger\hat{a} + \hbar\sum_{i,j} g_{ij}\left|i\right\rangle\left\langle j\right|\left(\hat{a} + \hat{a}^\dagger\right), \tag{3.10}$$

where the coupling constant is $\hbar g_{ij} = 2\beta e V_{rms}^0 \left\langle i\right|\hat{n}\left|j\right\rangle = \hbar g_{ij}^*$ and $\Omega_i\left|i\right\rangle$ are the bare eigenenergies and eigenvectors of the CPB. It can be easily appreciated that in order to achieve higher coupling regimes between the resonator and the qubit we need to increase the passive parameters $\beta$ and $V_{rms}^0$, as well as let the system work in the transmon regime, where the off-diagonal elements of the $\hat{n}$ operator become bigger.

#### Passive coupling parameters

By definition, we have that the ratio $\beta < 1$ and tends to one when $C_g \gg C_B + C_J$. On the other hand, the rms voltage $V_{rms}^0 \propto \frac{1}{L_r^{1/4}C_r^{3/4}}$ could be increased by designing a transmission line resonator with lower capacitance. If in addition we wanted to maintain the frequency of the oscillator at a constant value we should increase the inductance $L_r$. As the rms value has different powers for the inductance and capacitance this is actually possible. The task of increasing the inductance of superconducting wires is a very active research area in the field of quantum computing and in particular, current efforts are focused on modifying the kinetic inductance of the wires [41, 42]. Ideally, one would like to be able to engineer a resonator with independent $\omega_r$ and $V_{rms}^0$.

### Active coupling parameter

The active part of the coupling is the Cooper-pair number operator $\hat{n}$, whose values are dependent on the regime of $E_J/E_C$. In Fig. 3.2 we can see the off-diagonal elements calculated in the phase basis. It is interesting to notice that the coupling between nearest neighbour CPB eigenstates can be made of order unity in the transmon regime and increasingly big as the ratio $E_J/E_C$ grows, while further off-diagonal terms $\langle i|\hat{n}|j\rangle \to 0$ when $i \neq j+1$. It must be remember here, that as the coupling increases the transmon becomes more and more harmonic and the transmon will need more energy levels to be correctly described.

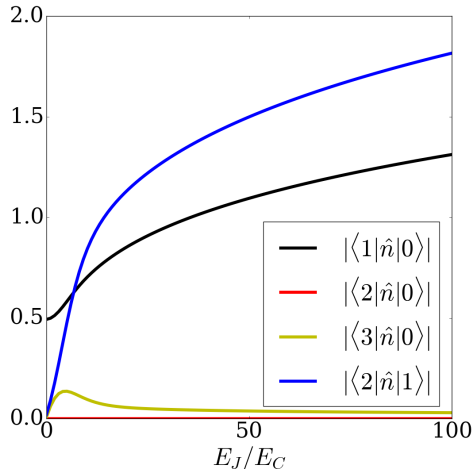


Figure 3.2: Off-diagonal matrix elements of the number operator as a function of the ratio $E_J/E_C$ with $n_g = 0.5$ calculated in the phase basis.

### 3.1.3 SQUID asymmetry and charge bias

In the derivation of Eq. (3.10) we assumed that the Josephson energies are symmetric but this is typically not the case. Given the current junction fabrication techniques, junction parameters can lead to asymmetries up to $d = \frac{E_{J1}-E_{J2}}{E_{J1}+E_{j2}} \approx \pm 10\%$. The case of the asymmetric junction was studied both in the CPB [43] and transmon regime [19]. We can replace the cosine term in Eq. (3.9) to obtain the Hamiltonian

$$H_{SQUID} = -E_{J1}\cos(\hat{\varphi}_1) - E_{J2}\cos(\hat{\varphi}_2), \tag{3.11}$$

where $\hat{\varphi}_{1,2}$ now describe the individual superconducting phase differences across the junctions with energies $E_{J1,2}$ respectively. By making use of the flux quantization along a superconducting ring [33] we get the relation

$$\varphi_1 - \varphi_2 = 2\pi m + 2\pi\frac{\Phi_{ext}}{\Phi_0}, \tag{3.12}$$

with integer $m$ and where $\Phi_{ext}$ denotes the external magnetic flux through the SQUID ring. We can define the effective phase difference of the device $\varphi_J = (\varphi_1 + \varphi_2)/2$ and using $E_{J\Sigma} = E_{J1} + E_{J2}$ rewrite the Hamiltonian (3.11) as

$$\begin{aligned} H_{SQUID} &= -E_{J\Sigma}\left[\cos(\pi\Phi_{ext}/\Phi_0)\cos\hat{\varphi}_J + d\sin(\pi\Phi_{ext}/\Phi_0)\sin\hat{\varphi}_J\right] \\ &= -E_{J\Sigma}\cos(\pi\Phi_{ext}/\Phi_0)\sqrt{1+d^2\tan^2(\pi\Phi_{ext}/\Phi_0)}\cos\left(\hat{\varphi}_J - \varphi_0\right) \\ &= -E_J\left(\Phi_{ext}\right)\cos\left(\hat{\varphi}_J - \varphi_0\right), \end{aligned} \tag{3.13}$$

where the phase $\varphi_0 = d\tan(\pi\Phi_{ext}/\Phi_0)$. This phase shift can be removed by shifting the variables if the external magnetic flux is constant but it could also be used to drive the qubit directly, see e.g. [44], where the external flux is varied to create photons.

In real experiments we always have asymmetric junctions, e.g. see next Sec. 3.3 to see the spectroscopy data of an experiment with a transmon qubit. Nevertheless, it can be seen in Fig. 3.3 that most of the effect is in the CPB regime. If we measure the energy levels of the bare SQUID close to the $\Phi_{ext} = 0.5$, the difference between a slightly asymmetric ($d < 1\%$) SQUID and a symmetric one is typically blurred out by the effect of the noise in the charge offset $n_g$ [19]. In Fig. 3.3 we see the discrepancy of the (a) energies and (b) coupling elements when

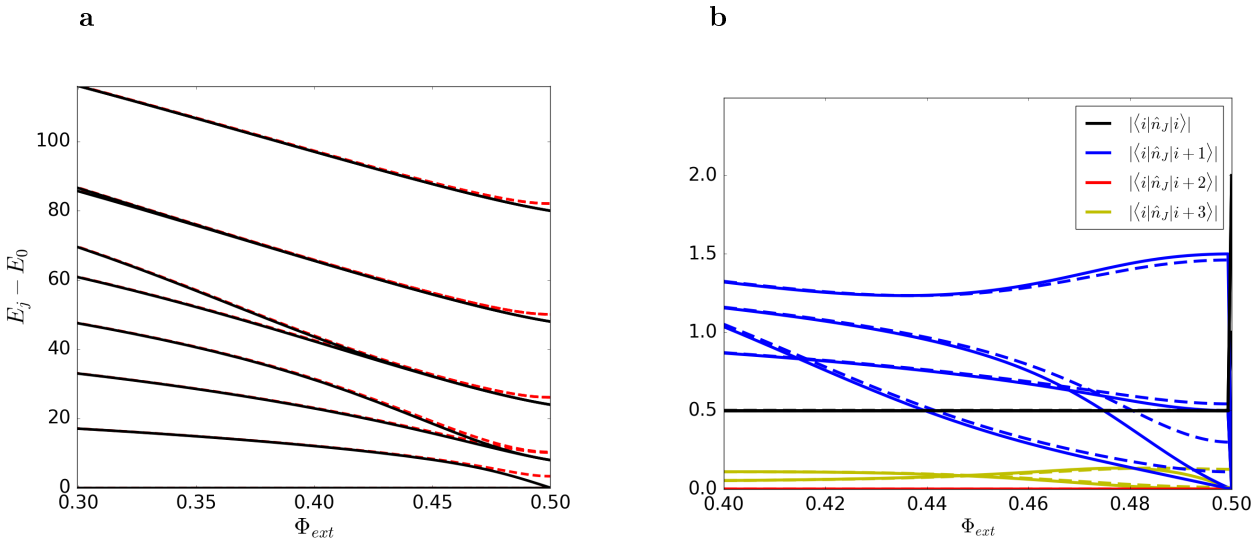


Figure 3.3: (**a**) Energy levels and (**b**) matrix elements of the number operator as a function of the external flux $\Phi_{ext}$ with $E_{J\Sigma}/E_C = 70$ with $n_g = 0.5$ and no asymmetry (solid lines) and $d = 5\%$ (dashed lines). As the external flux approaches $\Phi_{ext} \to 0.5$ ($E_J(\Phi_{ext}) \to 0$) the discrepancy increases.

the qubit is pushed towards the CPB regime with an asymmetry of $d = 5\%$ compared to the symmetric case.

In Fig. 3.3 we also see that the charge bias $n_g$ introduces a diagonal component in the coupling. The Cooper-pair number operator $|\langle i|\hat{n}_J|i\rangle| \to n_g$ as $E_J/E_C \to \infty$, something that can be easily proven performing a gauge transformation where $\hat{n}_J \to \hat{n}_J - n_g$.

## 3.2 New circuit model of a transmon qubit

In order to investigate the possibility of reaching the USC regime with the transmon we propose the simple circuit model of Fig. 3.4. It consists of a homogeneous transmission line resonator $(L_0, C_0)$ shorted to ground on one side ($x = 0$) and capacitively coupled ($C_g$) to a Josephson junction $(E_J, C_J)$ at the other end ($x = l$).

### 3.2.1 Lagrangian formalism

Following Secs. (3.1) and (2.2.2) the Lagrangian of the circuit in Fig. (3.4) can be written as

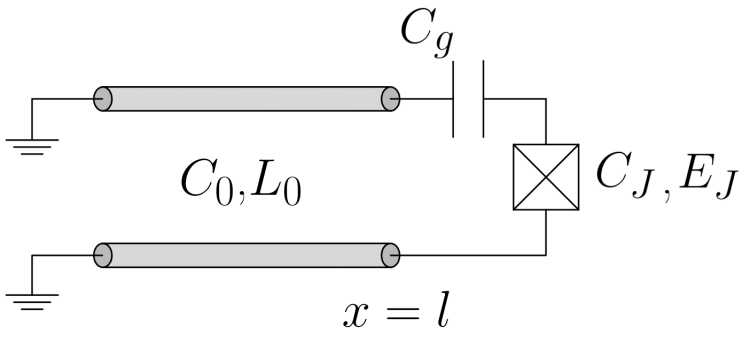


Figure 3.4: Transmon qubit ($C_J$, $E_J$) capacitively coupled ($C_g$) to a homogeneous transmission line resonator of capacitance and inductance per unit length $C_0$ and $L_0$ and total length $l$.

$$L = \int_0^l dx \left( \frac{C_0}{2} \left( \dot{\Phi}(x,t) \right)^2 - \frac{1}{2L_0} \left( \Phi'(x,t) \right)^2 \right) + \frac{C_g}{2} \left( \dot{\Phi}(l,t) - \dot{\phi}_J \right)^2 + \frac{C_J}{2} \dot{\phi}_J^2 + E_J \cos\left(2\pi\phi_J/\Phi_0\right), \tag{3.14}$$

where $\Phi(x,t)$ is again the continuous flux variable along the transmission line resonator of length $l$, and $\phi_J$ is the flux across the Josephson junction ($C_J$, $E_J$). To apply the method of canonical quantization we must find the normal modes of the transmission line resonator-capacitance subsystem. We vary the action associated with $\mathcal{L}$ for the flux field $\Phi(x,t)$ and get its equations of motion and boundary conditions, see Subsec. 2.2.2,

$$\ddot{\Phi}(x,t) - \frac{1}{C_0 L_0} \Phi''(x,t) = 0, \tag{3.15}$$

$$\Phi(0,t) = 0, \tag{3.16}$$

$$\ddot{\Phi}(l,t) + \frac{\Phi'(l,t)}{C_g L_0} = \ddot{\phi}_J(t). \tag{3.17}$$

Following [45], we expand the fields $\Phi(x,t) = \sum_n \psi_n(t)\, u_n(x)$ into a basis $\{u_n(x)\}$ for the homogeneous problem ($\dot{\Phi}_J = 0$) to decouple the above Eq. (3.15). Substituting the above into the homogeneous Eqs. (3.15)-(3.17), we derive

$$\frac{\ddot{\psi}_n(t)}{\psi_n(t)} = -\omega_n^2, \tag{3.18}$$

$$\frac{1}{C_0 u_n(x)} \left( \frac{u_n'(x)}{L_0} \right)' = -\omega_n^2, \tag{3.19}$$

$$u_n(0) = 0, \tag{3.20}$$

$$-\omega_n^2\, u_n(l) + \frac{1}{C_g\, L_0} u_n'(l) = 0. \tag{3.21}$$

The above Eqs. (3.19)-(3.21) for $u_n(x)$ set up a Sturm-Liouville-like eigenvalue problem with the eigenvalue parameter in the boundary conditions [46]. Applying Green's formula to this set of equations we find an orthogonality condition for the eigenfunctions

$$\int_0^l dx\, C_0 u_n(x) u_m(x) + C_g u_n(l) u_m(l) = \delta_{nm}\chi_n, \tag{3.22}$$

where $\chi_n$ is a normalisation factor that can be freely chosen for each mode. For convenience, we will set it equal to the total capacitance of the transmission line plus the coupling capacitance $C_\Sigma$,

$$\chi_n \Longleftrightarrow C_\Sigma \equiv \int_0^l dx\, C_0 + C_g = C_0 l + C_g. \tag{3.23}$$

We emphasise here that the basis functions $\{u_n(x)\}$ live in the weighted-space of double integrable functions $L^2([0,l], C_0)$ that is unitarily equivalent to $L^2([0,l])$, see [46]. Eqs. (3.19) and (3.20) suggest a harmonic solution of the type

$$u_n(x) = A_n \sin(k_n x), \quad 0 \leq x < l^-, \tag{3.24}$$

where $k_n \equiv \omega_n/\nu$ is the mode wave number and $\nu \equiv 1/\sqrt{L_0 C_0}$ the group velocity of the wave in the line [30]. Inserting the ansatz solution in (3.21), we find the transcendental equation for the wave numbers

$$\frac{C_0}{C_g k_n} = \tan(k_n l). \tag{3.25}$$

The amplitudes of the different wave numbers are found by inserting (3.24) in the orthonormality condition

$$A_n = \sqrt{2C_\Sigma}\left(C_0 l + \frac{C_g C_0^2}{C_0^2 + (C_g k_n)^2}\right)^{-1/2}. \tag{3.26}$$

See App. A.1 for the solution of the full problem. Finally, we can substitute the orthonormality condition (3.22, 3.23) of the eigenfunctions in (3.14), and obtain the Lagrangian (see App. A.2 for the derivation),

$$L = \sum_n \left(\frac{C_\Sigma}{2}\dot{\psi}_n^2 - \frac{1}{2L_n}\psi_n^2 - C_g \dot{\psi}_n u_n(l)\dot{\phi}_J\right) + \frac{(C_J + C_g)}{2}\dot{\phi}_J^2 + E_J \cos\left(2\pi\phi_J/\Phi_0\right), \tag{3.27}$$

where $L_n^{-1} \equiv \omega_n^2 C_\Sigma$. The Lagrangian (3.27) is composed of an infinitely discrete subsystem attached to an anharmonic one.

### 3.2.2 Hamiltonian formalism

Once we have a Lagrangian with a discrete set of degrees of freedom we can apply the Legendre transformation to derive a Hamiltonian. In order to simplify the calculus we do the following change of variables

$$\Psi_n = \sqrt{C_\Sigma}\psi_n \tag{3.28}$$

$$\Phi_J = \sqrt{C_G}\phi_J \tag{3.29}$$

where $C_G \equiv C_J + C_g$. The Lagrangian transforms to

$$L = \sum_n \frac{1}{2}\left(\dot{\Psi}_n^2 - \omega_n^2 \Psi_n^2 - 2\alpha_n \dot{\Psi}_n \dot{\Phi}_J\right) + \frac{1}{2}\dot{\Phi}_J^2 + E_J \cos\left(2\pi\Phi_J/\sqrt{C_G}\phi_0\right) \tag{3.30}$$

with $\alpha_n \equiv C_g u_n(l)/\sqrt{C_\Sigma C_G}$. We then do a Legendre transformation to Eq. (3.30) where the charges (conjugate variables to the fluxes) are

$$Q_n \equiv \frac{\partial L}{\partial \dot{\Psi}_n} = \dot{\Psi}_n - \alpha_n \dot{\Phi}_J, \tag{3.31}$$

$$Q_J \equiv \frac{\partial L}{\partial \dot{\Phi}_J} = \dot{\Phi}_J - \sum_n \alpha_n \dot{\Psi}_n, \tag{3.32}$$

and obtain the Hamiltonian

$$H = \sum_n \frac{1}{2}\left(Q_n^2 + \omega_n^2 \Psi_n^2\right) + \frac{1}{2(1-\alpha_S^2)}\left(Q_J + \sum_n \alpha_n Q_n\right)^2 - E_J \cos\left(2\pi\Phi_J/\sqrt{C_G}\Phi_0\right). \tag{3.33}$$

Here $\alpha_S^2 \equiv \sum_n \alpha_n^2$ is a convergent bounded sum for the $k_n$ and $u_n(l)$ of this problem, see App. A.3. It must also be noted that $\alpha_S^2 \leq 1$, as we started from a Lagrangian description of a physical system (3.14) whose kinetic matrix is (semi-)positive definite. The case where $\alpha_S^2 = 1$ would correspond to a redundant degree of freedom in the description.

### 3.2.3 Normal mode structure

The Legendre transformation mixes the former normal modes

$$H = \sum_n \frac{1}{2}\left(\omega_n^2 \tilde{Q}_n^2 + \tilde{\Psi}_n^2\right) + \frac{1}{2(1-\alpha_S^2)}\left(Q_J + \sum_n \tilde{\alpha}_n \tilde{Q}_n\right)^2 - E_J \cos\left(2\pi\Phi_J/\sqrt{C_G}\Phi_0\right), \tag{3.34}$$

where we have made the canonical transformation $\tilde{\Psi}_n \equiv \omega_n \Psi_n$, $\tilde{Q}_n \equiv Q_n/\omega_n$ and defined $\tilde{\alpha}_n \equiv \alpha_n \omega_n$. The Hamiltonian written in matrix form is then

$$\begin{aligned} H \;&= \frac{1}{2}\vec{\tilde{Q}}^T K \vec{\tilde{Q}} + \frac{1}{2}\vec{\tilde{\Psi}}^T \vec{\tilde{\Psi}} + \frac{\vec{\tilde{\alpha}}^T}{(1-\alpha_S^2)}\vec{\tilde{Q}} Q_J \\ &+ \frac{1}{2(1-\alpha_S^2)}\left(Q_J + Q_{DC}\right)^2 - E_J \cos\left(2\pi\Phi_J/\sqrt{C_G}\Phi_0\right), \end{aligned} \tag{3.35}$$

where we have explicitly written the charge bias $Q_{DC}$, that comes from the dc-component of the flux modes $\Phi(x,t)$ (see App. A.1), with

$$K = \tfrac{1}{(1-\alpha_S^2)} \begin{pmatrix} (1-\alpha_S^2)\omega_1^2 + \tilde{\alpha}_1^2 & \tilde{\alpha}_1\tilde{\alpha}_2 & \tilde{\alpha}_1\tilde{\alpha}_3 & \cdots \\ \tilde{\alpha}_1\tilde{\alpha}_2 & (1-\alpha_S^2)\omega_2^2 + \tilde{\alpha}_2^2 & \tilde{\alpha}_2\tilde{\alpha}_3 & \cdots \\ \tilde{\alpha}_1\tilde{\alpha}_3 & \tilde{\alpha}_2\tilde{\alpha}_3 & (1-\alpha_S^2)\omega_3^2 + \tilde{\alpha}_3^2 & \\ \vdots & \vdots & & \ddots \end{pmatrix}, \tag{3.36}$$

and being the vectors $\vec{\tilde{Q}} = (\tilde{Q}_1, \tilde{Q}_2, ...)$, $\vec{\tilde{\Psi}} = (\tilde{\Psi}_1, \tilde{\Psi}_2, ...)$ and $\vec{\tilde{\alpha}} = (\tilde{\alpha}_1, \tilde{\alpha}_2, ...)$. Having studied the convergence issues of the problem, we truncate the number of modes in the resonator to $p$, find the orthogonal matrix $U$ that diagonalizes $K$, i.e. $W \equiv U^T K U = \mathrm{diag}(\tilde{\omega}_1^2, \tilde{\omega}_2^2, ..., \tilde{\omega}_p^2)$, and do the new canonical transformation $\vec{\xi} \equiv U^T \vec{\tilde{Q}}$, $\vec{\tau} \equiv U^T \vec{\tilde{\Psi}}$. We undo also the transformation $\phi_J = C_G^{-1/2}\Phi_J$, $q_J = C_G^{1/2} Q_J$ and $q_{DC} = C_G^{1/2} Q_{DC}$

$$H \approx \tfrac{1}{2}\vec{\xi}^T W \vec{\xi} + \tfrac{1}{2}\vec{\tau}^T\vec{\tau} + \vec{\beta}^T\vec{\xi} q_J + \tfrac{1}{2(1-\alpha_T^2)C_G}\left(q_J - q_{DC}\right)^2 - E_J \cos\left(2\pi\phi_J/\Phi_0\right), \tag{3.37}$$

where $\vec{\beta} \equiv \frac{1}{(1-\alpha_S^2)C_G^{1/2}} U^T \vec{\tilde{\alpha}}$. We quantize the system, imposing commutation relations $[\tau_n, \xi_n] = i\hbar$ and introduce creation and annihilation operators $a_n$ and $a_n^\dagger$ for the harmonic modes

$$\hat{\tau}_n = i\sqrt{\frac{\hbar\tilde{\omega}_n}{2}}\left(a_n - a_n^\dagger\right), \tag{3.38}$$

$$\hat{\xi}_n = \sqrt{\frac{\hbar}{2\tilde{\omega}_n}}\left(a_n + a_n^\dagger\right), \tag{3.39}$$

where $\left[a_n, a_m^\dagger\right] = \delta_{nm}$. The Hamiltonian can then be written as

$$\begin{aligned} H &= \sum_n \hbar\tilde{\omega}_n\left(a_n^\dagger a_n + \frac{1}{2}\right) + \sum_n \eta_n\left(a_n + a_n^\dagger\right) n_J \\ &+ 4E_C^{'}\left(n_J - n_{DC}\right)^2 - E_J\cos\left(\varphi_J\right), \end{aligned} \tag{3.40}$$

where the charge energy is $E_C^{'} = e^2/2(1-\alpha_S^2)C_G$ and the Josephson phase $\varphi_J = 2\pi\phi_J/\Phi_0$. Note that the typical charging energy of the transmon Hamiltonian $E_C = e^2/2C_G$ is strongly modified by the presence of the resonator coupled to it through the convergent series $\alpha_S^2$. We also have defined the coupling parameters as

$$\begin{aligned} \eta_n &\equiv 2e\beta_n\sqrt{\hbar/2\tilde{\omega}_n} \\ &= \frac{eC_g}{(1-\alpha_S^2)C_G}\sqrt{\frac{2\hbar}{C_\Sigma\tilde{\omega}_n}}\sum_j U_{jn}u_j(l)\omega_j. \end{aligned} \tag{3.41}$$

Due to the fact that the above expression depends non-trivially on the input parameters, we do not have at this point an analytical prescription on how to increase the coupling parameters for the lower modes. Nevertheless, now that we have a full quantum description of this circuit model, we will resort to numerics to test its potential to describe recent experimental data shared by the group of Pr. Gary Steele, where a dc-SQUID in the transmon configuration has been ultrastrongly coupled to a transmission line resonator.

## 3.3 Experimental aspects of a transmon in the USC regime

Having reviewed the original transmon system and presented the new multimode model, we now introduce a new experimental setup that has been developed in the laboratory of Pr. Gary Steele to achieve the USC regime with the transmon. We check that a heuristic model of a multimode resonator capacitively coupled to a SQUID suffices to describe the spectrum of this experiment. In a second step, we verify that fitted Hamiltonian parameters agree very well with our model for values of the circuit close to their original design. Motivated by the success of the model, we study the distribution of population in the qubit and resonator modes, as the external flux is varied from the CPB ($E_J \sim E_C$) to the transmon regime ($E_J/E_C \gg 1$). We show free evolution of simple initial states, where full population inversion between the first levels of the transmon and the resonator modes can be appreciated. Results are compared with a simplified model where a rotating wave approximation has been performed to all counter-rotating terms in the Hamiltonian. In a final step, we verify that fitted Hamiltonian parameters for the heuristic model, agree very well with our model for values of the circuital elements close to their original design.

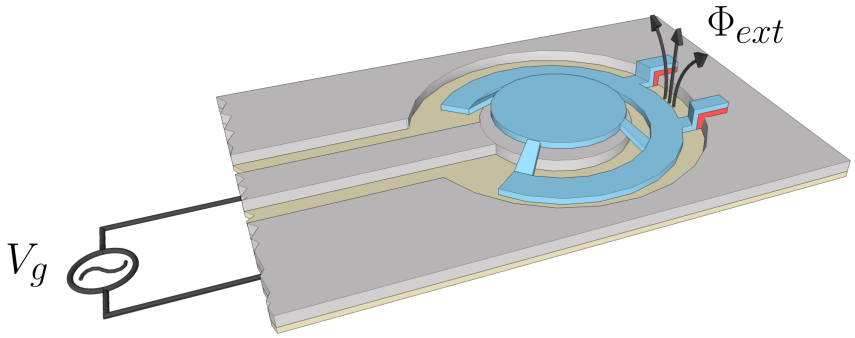


Figure 3.5: Artistic schematic of the real experimental chip that has been designed in Delft. A dc-SQUID is formed with a piece of superconductor (blue) above the ground superconducting plate (grey) with insulators (red) between them. The centre line of the transmission line resonator is coupled to the SQUID through a vacuum-gap capacitor formed by a modification of the shape of the center superconductor and the round (blue) plate suspended above it. The SQUID is threaded by an external flux $\Phi_{ext}$ and the whole system is externally controlled by pulses sent from a voltage source $V_g$ at the beginning of the line.

### 3.3.1 Experimental design

Our collaborators in the laboratory of Gary Steele have designed a system consisting of a SQUID coupled to a $\lambda/4$-transmission line resonator of total length $l_{tot} = 4.7\,\mathrm{mm}$, and characteristic impedance $Z_0 = 50\Omega$ through a big vacuum-gap capacitor of radius $R \sim 15\mu\mathrm{m}$. An artistic schematic of the real circuit is shown in Fig. 3.5.

### 3.3.2 Energy spectrum

In analogy with Subsecs. 2.2.2 and 3.1.1, we can write Hamiltonians for the uncoupled transmission line and SQUID subsystems as

$$H_{SQUID} = 4E_C\left(n_J - n_g\right)^2 - E_{J\Sigma}\cos\left(\varphi_{ext}\right)\cos\left(\varphi_J\right) - dE_{J\Sigma}\sin\left(\varphi_{ext}\right)\sin\left(\varphi_J\right), \quad (3.42)$$

$$H_{TL} = \sum_n \hbar\omega_n\left(a_n^\dagger a_n + \frac{1}{2}\right). \quad (3.43)$$

Assuming that the capacitance does not modify the resonator geometry, the wave numbers of the bosonic modes are $k_n = (2n+1)\,\pi/2l_{tot}$. As we have seen in Eq. (3.40), a heuristic model for a capactive coupling between the SQUID and the multimode resonator could be generally written as

$$H_{int} = \sum_n \eta_n\left(a_n + a_n^\dagger\right) n_J, \quad (3.44)$$

such that the total heuristic Hamiltonian is then

$$H = H_{SQUID} + H_{TL} + H_{int}. \quad (3.45)$$

If we truncate the CPB system to its two lowest energy levels, it then becomes the Hamiltonian proposed by Houck et al. in [47] to describe a transmon qubit coupled to a resonator. Writing the CPB operators in their diagonal basis we put the Hamiltonian in the multilevel multimode cQED form

$$H = \hbar \sum_i \Omega_i(\Phi_{ext})\sigma_{ii} + \sum_n \hbar\omega_n \left(a_n^\dagger a_n + \frac{1}{2}\right) + \hbar \sum_{i,j} g_{ij}(\Phi_{ext})\sigma_{ij} \sum_n \eta_n \left(a_n + a_n^\dagger\right), \quad (3.46)$$

with $\sigma_{ij} = |i\rangle\langle j|$ and the eigenenergies $\Omega_i$, and couplings $g_{ij}$ depending on the external flux $\Phi_{ext}$.

Spectroscopic measurements of a circuit in the frequency range $(3.8 - 4.5)$ GHz and $(4.5 - 15)$ GHz are shown in Figs. 3.6 and 3.7 respectively as a function of the external flux. The dashed lines correspond to the fitted energy spectrum of the Hamiltonian (3.46), with the parameters shown in Table 3.1. This numerical fitting was done by truncating the number of modes in the resonator to two and the number of energy levels of the transmon to four, and together with most of the the numerical diagonalizations and time evolutions in this thesis, was performed with the QuTiP package in Python [48]. It can be appreciated that the second transmission line mode has $\omega_1 = 12.656\,\text{GHz} \neq 3\omega_0$, as it should exactly be for a perfectly harmonic transmission line. A simple explanation could be that higher modes induce a Stark-shift on this second mode.

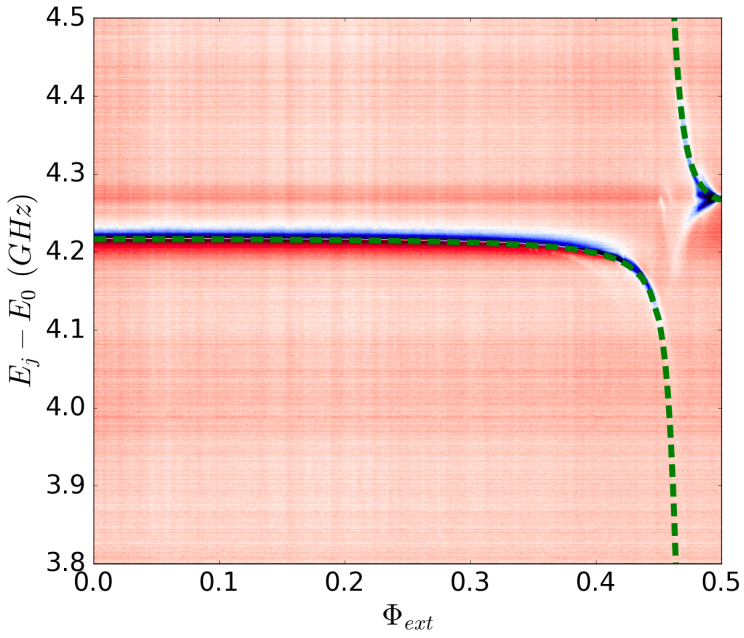


Figure 3.6: Transmission spectrum of the experiment in the frequency range $(3.8 - 4.5)$ GHz [49]. The green dashed lines are the first and second eigenvalues of the Hamiltonian (3.46) with the parameters in Table 3.1. At $\Phi_{ext} \approx 0.46(\Phi_0)$ we see the Rabi splitting between the first CPB transition and the first bosonic mode.

### SQUID regimes and rotating wave approximation

When the SQUID is threaded by an external flux $\Phi_{ext} \approx 0.46\,(0.2)\,\Phi_0$ we see that the frequencies of the first transition in the CPB (transmon) and of the first (second) resonator mode match and thus a Rabi splitting occurs. We define a total coupling constant $s_{01} \equiv g_{01}(0.46\Phi_0)\eta_0 = 316$ MHz in the CPB regime which yields a relation between the coupling and the frequency of the resonator mode of $s_{01}/\omega_0 = 0.074$. Something similar happens for the transmon regime with

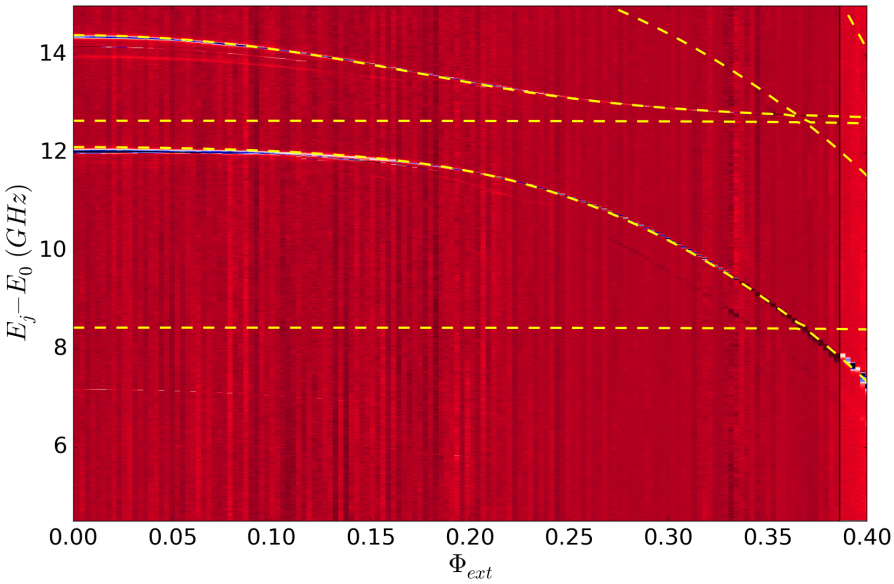


Figure 3.7: Transmission spectrum in the frequency range $(4.5 - 15)$ GHz [49]. The dashed lines are the eigenvalues $E_j - E_0$ with $j \in \{1 - 6\}$ of the Hamiltonian (3.46) with parameters in Table 3.1. At $\Phi_{ext} \approx 0.2(\Phi_0)$ we see the Rabi splitting between the first CPB transition and the second bosonic mode. First and third flat lines about $\Phi_{ext} = (0 - 0.35)$ are eigenstates $|\Psi_{1(3)}\rangle = |0, 1(2), 0\rangle$ (kets in $\mathcal{H}_{CPB} \otimes \mathcal{H}_0 \otimes \mathcal{H}_1$) with transition amplitude $\langle\Psi_j|a_0 + a_0^\dagger|\Psi_j\rangle = 0$, that cannot be experimentally observed. Spurious unknown transmission is also observed around 14 GHz.

| Parameter | Value |
|---|---|
| **Transmission line resonator** | |
| Frequency $\omega_0/2\pi$ | 4.268 GHz |
| Frequency $\omega_1/2\pi$ | 12.656 GHz |
| **Vacuum gap capacitor** | |
| Coupling $\eta_0/2\pi$ | 470 MHz |
| Coupling $\eta_1/2\pi$ | 800 MHz |
| **SQUID** | |
| Charge energy $E_C/2\pi$ | 606 MHz |
| Josephson energy $E_{J\Sigma}/2\pi$ | 43.5 GHz |
| Charge offset $n_g$ | 0.409 |
| Asymmetry $d$ | $< 0.1\%$ |

Table 3.1: Used parameters to fit the energy spectrum in Figs. 3.6 and 3.7 with the heuristic Hamiltonian (3.46). It can be spotted, that the second mode frequency $\omega_1$ is not the purely harmonic one where $\omega_n = (2n + 1)\omega_0$.

the second mode coupling parameter $t_{01} \equiv g_{01}(0.18\,\Phi_0)\eta_1 = 915\,\text{MHz}$ and ratio $t_{01}/\omega_1 = 0.073$. The system is in the USC regime $s_{01}/\omega_0 = 0.13$ with respect to the first mode at $\Phi_{ext} = 0$, but this mode frequency is really off-resonant with respect to the transition $\Omega_{01}$. Therefore, making a rotating wave approximation (RWA), retaining only the excitation number conservative terms $\left(\sigma_{ij}a_n + \sigma_{ji}a_n^\dagger\right)$ with $i > j$, will behave very similarly, see Fig 3.9 for comparison of the free dynamics evolution with and without the RWA.

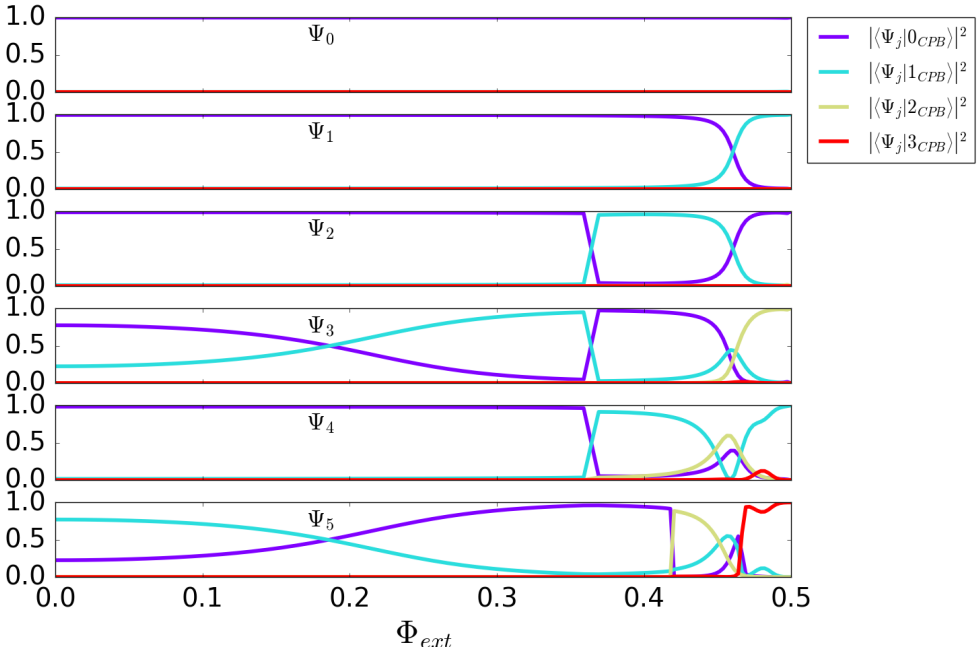


Figure 3.8: Fock state population in the CPB as a function of the external flux for the first six eigenvectors $|\Psi_i\rangle$ $(i \in \{0-5\})$. Populations of the $4th$ level only becomes apparent in $|\Psi_{5,6}\rangle$ at the Cooper-pair box regime. Smooth level crossings of fock states $|0\rangle$ and $|1\rangle$ in $|\Psi_{1,2}\rangle$ at $\Phi_{ext} \approx 0.46\Phi_0$ and in $|\Psi_{3,5}\rangle$ happen at $\Phi_{ext} \approx 0.18\Phi_0$, which correspond to first CPB transition being resonant with the first and second mode respectively.

### Populations

We verify the truncation to the four first energy levels of the CPB by plotting the populations of those levels in the eigenvectors of the full Hamiltonian (3.46), see Fig. 3.8. It can be checked that for the first six eigenvectors $|\Psi_i\rangle$ $(i \in \{0-5\})$, populations of the $4th$ level only become apparent in the last two of them close to the CPB regime. For the part of the spectrum of Fig. 3.6 $(3.8 - 4.5\,\text{GHz})$ only the first two transitions $E_{10}$, $E_{20}$ can be seen and there is no need for more levels. The same can be seen in Fig. 3.7, where in the range of $\Phi_{ext} = (0,\, 0.4\Phi_0)$ we could only see up to the $E_{50}$ transition, but there is no population above the second level of the transmon.

At $\Phi_{ext} \approx 0.46\Phi_0$ we see smooth state crossings $|0,1,0\rangle \leftrightarrow |1,0,0\rangle$, where the kets belong to the Hilbert space $\mathcal{H}_{CPB} \otimes \mathcal{H}_0 \otimes \mathcal{H}_1$, in eigenstates $|\Psi_{1,2}\rangle$, as a result of the energy of the first transition of the CPB being resonant with that of the first mode in the resonator. The same thing happens at $\Phi_{ext} \approx 0.186\Phi_0$, with states $|\Psi_{3,5}\rangle$ and the second mode of the resonator $(|0,0,1\rangle \leftrightarrow |1,0,0\rangle)$. At $\Phi_{ext} \approx 0.37\Phi_0$ populations of $(|0,2,0\rangle \leftrightarrow |1,0,0\rangle)$ abruptly cross each other in the $|\Psi_{3,4}\rangle$ (no gap opens in the spectrum of Fig. 3.7). This is due to the fact that

there is no two-photon interaction of the form $(\sigma_{01} + \sigma_{10})\left(a^2 + (a^\dagger)^2\right)$ in our Hamiltonian and double photon interaction is prohibited by symmetry.

### Free evolution dynamics

We finish exploiting this experimental setup by showing the free dynamics of simple initial states, under the fitted Hamiltonian at the interesting eigenstates avoided-crossing points. Occupation numbers $\langle \hat{n}_i \rangle$ in Fig. 3.9(a) show full Rabi oscillations between the first (second) mode of the resonator and the first transition of the CPB (transmon) at $\Phi_{ext} = 0.4605\,(0.18)\,\Phi_0$ when the system is initialised in $|\Psi(0)\rangle = |1,0,0\rangle$. The expectation value of the quadrature components $\langle \hat{X}_i = a_i + a_i^\dagger \rangle$ and $\langle \hat{P}_i = i(a_i^\dagger - a_i) \rangle$ of the Rabi-flopping mode show a modulated oscillatory behaviour. At $\Phi_{ext} = 0.186$, $\langle \hat{X}_2 \rangle$ becomes minimum when all the population is in the harmonic mode. The quadrature components are not zero because the coupling to the bosonic modes is not purely off-diagonal, i.e. $g_{ii}\,(\Phi_{ext}) \neq 0$, $\forall \Phi_{ext} \in [0, \Phi_0/2)$, something that only occurs when $n_g = 0$ and there is negligible asymmetry, as discussed in Subsec. 3.3. Furthermore, $g_{ii}\,(0.186\Phi_0)$ is constant for all $i$ whereas $g_{ii}\,(0.46\Phi_0)$ is not, and that is why the quadratures complete a full cycle in each Rabi flop in one case, and not in the other. It must be also noticed that when performing the RWA approximation discussed above, the Rabi-flops are very well approximated, a signature of the system behaving in the non-resonant USC regime.

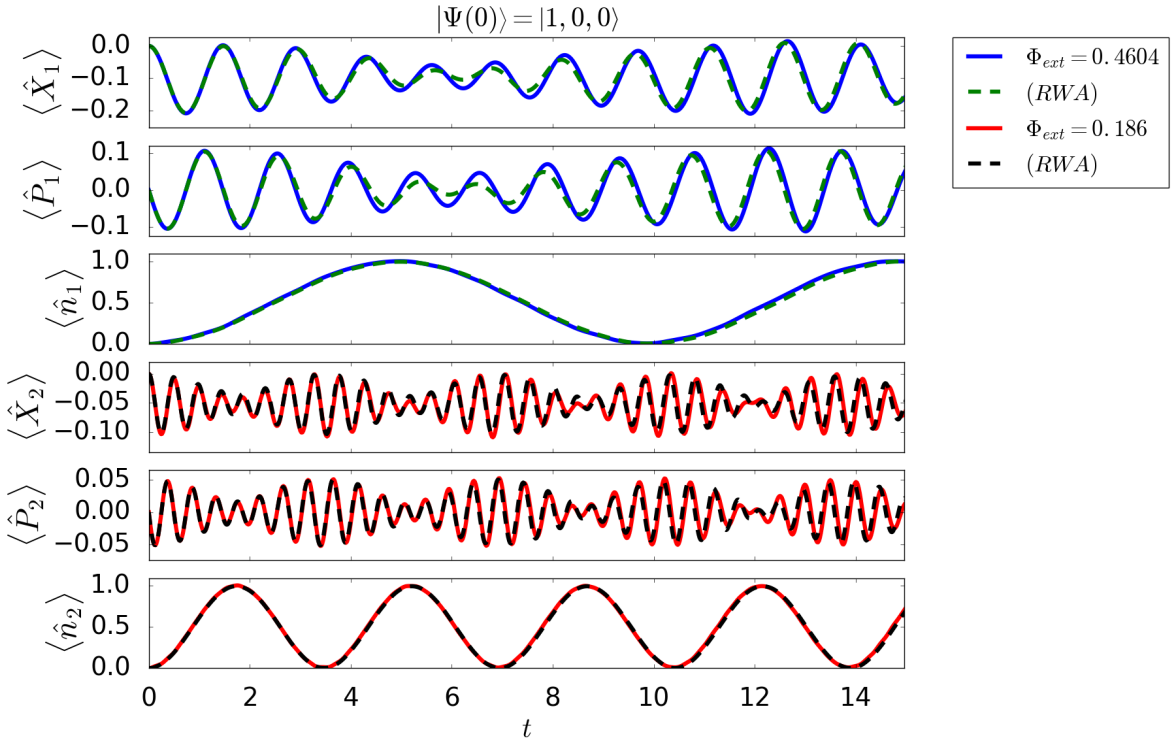


Figure 3.9: Free evolution of the initial state $|\Psi(0)\rangle = |1,0,0\rangle$ at the two level crossing points $\Phi_{ext} = 0.4605\,(0.18)\,\Phi_0$. The rotating wave approximation performed approximates very well the full Hamiltonian. The oscillations in the quadratures are smaller when the population in the bosonic modes becomes maximum.

### 3.3.3 New circuit model fit

Having found the effective set of parameters for the heuristic model that fits the spectrum, we now try to adjust those values to the new circuit model Hamiltonian 3.40. The new fitting process consists in matching the set of frequencies ($\omega_0$, $\eta_0$, $E_C^{'}$), leaving as free parameters: (i) the circuit capacitances $C_J$, $C_g$ (note that $C_J$ includes the parallel capacitances of both junctions in the SQUID), and (ii) an effective capacitance length $d$, that will be subtracted from the transmission line length ($l = l_{tot} - d$), in order to absorb extra effects (e.g. border currents) that happen in the real circuit, see Fig. 3.5. Note, that the Josephson potential is not modified by the flux variables, thus we can exchange the Josephson energy $E_J$ for $E_{J\Sigma}(\Phi_{ext})$ as in Eq. (3.13).

| **Parameter** | Value | | |
|---|---|---|---|
| **Fixed** | | | |
| Capacitance per unit length (designed) $C_0$ | 249 pF/m | | |
| Inductance per unit length (designed) $L_0$ | 623 nH/m | | |
| Total length (designed) $l_{tot}$ | 4.7 mm | | |
| Number of modes $N$ | 4 | 800 | 1500 |
| **Free** | | | |
| Josephson capacitance $C_J$ | 13.2 fF | 31.7 fF | 31.8 fF |
| Coupling capacitance $C_g$ | 22.0 fF | 52.9 fF | 53.15 fF |
| Effective capacitance length $d$ | 30.06 $\mu$m | 76.6 $\mu$m | 76.9 $\mu$m |
| **Fitted** | | | |
| Frequency first mode $\tilde{\omega}_0 \leftrightarrow \omega_0$ | $2\pi \times 4.268$ GHz | | |
| Coupling first mode $\eta_0 \leftrightarrow \eta_0$ | $2\pi \times 470$ MHz | | |
| Charge energy $E_C^{'} \leftrightarrow E_C$ | $2\pi \times 606$ MHz | | |
| **Automatic** | | | |
| Frequency second mode $\tilde{\omega}_1 \leftrightarrow \omega_1$ | $2\pi \times 12.8$ GHz | | |
| Coupling second mode $\eta_1 \leftrightarrow \eta_1$ | $2\pi \times 821.0$ MHz | $2\pi \times 811.8$ MHz | |
| Convergent sum $\alpha_S^2$ | 0.1 | 0.622 | 0.624 |

Table 3.2: Circuit parameters required to adjust the frequencies $\tilde{\omega}_0$, $\eta_0$ and $E_C^{'}$ ($\omega_0$, $\eta_0$ and $E_C$ in the heuristic model, which in turn fits the spectrum in Fig. 3.5) with the fixed parameters, after a square-root minimization of the free parameters.

In Table 3.2, we show the results of the numerical optimisation process. It is interesting to note, that if we truncate the number of resonator modes to a small $N$ (see 3.40), the effective capacitance length $d$ needed to fit the three values above, becomes very close to the diameter of the designed capacitor, and specifically for $N = 4$ becomes almost exactly that $\varnothing = 30.06\mu$m. Furthermore, with that specific set of parameters, the total capacitance in parallel to the SQUID needed in that fit is extremely close to the one originally designed, readily $C_J \approx 11$ fF. On the other hand, as we have pointed out in App. A.3, the convergence of the $\alpha_S^2$ parameter implies a finite convergence of all the free circuit parameters, for the same set of fitted parameters, as we increase $N$. In that case, the lumped capacitances of the circuit must be also increased in order to adjust the frequencies. One explanation for this slight difference in the free parameter $d$ required for fitting with respect to truncation of modes $N$, for the ratio of capacitances $C_g/C_0 l \approx 0.04$ that we have, the solution of the transcendental equation for the small wave numbers yields $k_n \approx (2n+1)\pi/2l$, see Fig. A.1. In other words, with such a small coupling capacitance, the smallest wave numbers barely change with respect to the open transmission line, see Sec. 2.2.2. The main disagreements that we encountered in the fits are: (i) that the

effective second mode frequency ($\omega_1$) used in the heuristic model is slightly shifted (+144 MHz) from the more harmonic result we get in the circuit model ($\tilde{\omega}_1$), and (ii) that its coupling $\eta_1$ to the SQUID is also overestimated by 2.6%. These results hint that this very simple model matches reasonably well the experimental data set.

An other way to model this system is making use of the blackbox quantization procedure [50], an approach that has proven to be very successful to explain and to engineer non trivial quantum states [51, 52]. The main drawback with such modelling is that it requires one to have a precise characterisation of the impedance matrix seen by the anharmonic subsystem (Josephson potential) which we lacked. In that context, the blackbox could be the transmission line resonator with the suspended capacitor, and the two output ports would be defined by the Josephson junctions and the entrance to the line seen by the voltage source ($V_g$ in Fig. 3.5). An open question would be, whether tracing out the upper bosonic modes in the resonator with a dispersive treatment could improve the fit.

To summarise, the circuit model that has been presented in Sec. 3.2 can be reduced to an effective one-dimensional model a real experiment, where a transmon qubit has been coupled to bosonic modes of transmission line resonator in the non-resonant perturbative USC regime. Furthermore, pushing the model to the limit of extremely high number of modes (way beyond the usual frequency ranges) can still be seen as an effective analog quantum simulator of this particular experiment. In order to test the validity of the model as a predictive tool for designing stronger couplings between a transmon qubit and resonator modes at resonance, we will require more data sets with several different parameters. In that sense, a deeper look into the behaviour of the coupling parameters $\eta_n$ will be required in order a get a more useful closed-form expression, see Eq. (3.41). Looking further in the future, it could be interesting to study new designs of transmission lines with inhomogeneous geometries to simulate specific field theories [53] with non trivial space-time curvatures [54, 55].

# Chapter 4

# Circuit QED in the USC and DSC regimes

This year has brought several outstanding experiments [56, 57, 58] in circuit QED. Different experimental groups have been able to couple superconducting flux qubits [40] to discrete [56, 57] and continuous [58] sets of bosonic modes in the USC and DSC [15] regimes. Furthermore, entering the perturbative USC regime has also been achieved with a transmon qubit and a multimode resonator, see Sec. 3.3. Motivated by the success of these results, we are going to study in this section a system with two bosonic modes coupled to a qutrit in a (i) transmon-like and (ii) CPB/flux qubit-like configurations, when the coupling of the first transition of the qutrit to the first mode goes from the USC to the DSC regime. We will also focus on a specific feature of this regime, namely the collapses and revivals of populations in the qutrit and the first bosonic mode. We will finally analyse how a more realistic transmon-like capacitive coupling model still allows us to see similar features.

## 4.1 Beyond the quantum Rabi model

In Sec. 3.3 we have shown how a SQUID subsystem truncated to few levels coupled to two resonator modes faithfully reproduces the spectrum of the experimental set up in Sec. 3.3. In that system, there was only a free parameter that could be actively tuned during the experiment, readily the external magnetic flux threading the loop of the SQUID $\Phi_{ext}$. We have seen that such a parameter controls both the energy level spacing of the anharmonic subsystem, and its coupling parameters to the bosonic modes. The theoretical model that we are going to now explore has the same terms of Eq. (3.46), but we are going to truncate the anharmonic system to three levels. In addition, we are going to depart from that specific circuit implementation, by allowing the coupling parameter to be tuned independently of the energy transitions. Specifically, we consider the Hamiltonian

$$H = \hbar \sum_{i=0}^{2} \Omega_i \sigma_{ii} + \sum_{n=0,1} \hbar \omega_n \left( a_n^\dagger a_n + \frac{1}{2} \right) + \hbar \sum_{i,j} g_{ij} \sigma_{ij} \sum_n \eta_n \left( a_n + a_n^\dagger \right). \tag{4.1}$$

The above Hamiltonian can be thought as an extension of the quantum Rabi model (QRM), however with two bosonic modes of creation and annihilation operators $a_{0,1}$ and $a_{0,1}^\dagger$ and frequencies $\omega_{0,1}$, and a qutrit with operators $\sigma_{ij} = |i\rangle \langle j|$ and frequencies $\Omega_i$, with $i, j \in \{g, e, f\}$, where $(g, e, f)$ stand for ground, first and second excited state. A linear capacitive coupling between both subsystems is parametrised by $\eta_n$ and $g_{ij}$. Following the multimode resonator case we will assume that $\omega_n = (2n+1)\omega_0$ and $\eta_n = \sqrt{2n+1}\eta_0$, see above Sec. 3.3. We will

only focus on the case where the first mode is resonant with the first transition of the qutrit, i.e. $\omega_0 = \Omega_{ge} \equiv \Omega_e - \Omega_g$. To simplify the model we will rewrite the coupling parameters as $s_{ij} \equiv \eta_0 g_{ij}$ and $t_{ij} \equiv \eta_1 g_{ij} = \sqrt{3} s_{ij}$, which shows there is only one set of independent coupling parameters $s_{ij}$. For simplicity we have set $\omega_0 = \Omega_{ge} = 1$ such that the Hamiltonian depends only on the $s_{ij}$ parameters.

### 4.1.1 Parameter configurations for the two-mode-qutrit system

We are going to distinguish between two possible coupling sets: (i) the off-diagonal configuration where $g_{ge} = g_{eg} = g_{ef} = g_{fe} = 1$ and $g_{ij} = 0$ for the rest, and the (ii) transmon-like configuration where $g_{ij} = \langle i|\hat{n}_J|j\rangle$, with $\hat{n}_J$ being the Cooper-pair number operator of an associated transmon circuit, with eigenenergies and eigenvectors $\Omega_i$ and $|i\rangle$ respectively. We will focus first on the study of the first configuration, leaving the second for further comparison in Sec 4.4 as a simple modification that could be more easily implemented in circuit QED experiments. These coupling configurations will be studied for two different qutrit species:

1. *CPB-like* qutrit: the second transition is far off resonance with the first transition $\Omega_{ef} = \Omega_f - \Omega_e \approx 8.5\Omega_{ge}$, see Fig. 4.1(a). This model could be reproduced with a flux qubit or a CPB at $E_J/E_C = 1$.

2. *Transmon-like* qutrit: the second transition is close to the first transition $\Omega_{ef} \approx 0.90\Omega_{ge}$, see Fig. 4.1(b). The energy transitions correspond to a transmon working at $E_J/E_C = 15$, close to its maximum of anharmonicity [19].

We have done a study of the models from the the USC to the DSC regime between the coupling to the first transition of the qutrit and the frequency of the first mode of the resonator, i.e. in the range $0.1 < s_{ge}/\omega_0 < 1.6$.

### 4.1.2 Considerations on the perturbative USC regime

In the quantum Rabi model

$$H_R = \hbar\frac{\Omega_q}{2}\sigma_z + \hbar\omega_r a^\dagger a + \hbar g\sigma_x\left(a + a^\dagger\right), \tag{4.2}$$

where the coupling constant $g$ gets close to the order of magnitude of the qubit $\omega_q$ and resonator $\omega_r$ frequencies, a perturbative transformation $H_{BS} = e^S H_R e^{-S}$ with $S = \gamma(a\sigma_- + a^\dagger\sigma_+)$ when $\gamma = g/(\omega_q + \omega_r) \ll 1$ (perturbative USC regime), can eliminate the counter-rotating terms [59, 60]. To second order in $\gamma$ the Hamiltonian transforms into

$$H_{BS} = \tfrac{\hbar\Omega_q}{2}\sigma_z + \hbar\omega n + \hbar\omega_{BS}\left[\sigma_z\left(n + \tfrac{1}{2}\right) - \tfrac{1}{2}\right] + \hbar g(\hat{n})\left(a^\dagger\sigma_- + a\sigma_+\right), \tag{4.3}$$

$$g(\hat{n}) \equiv -g\left[1 - n\omega_{BS}/(\omega_q + \omega_r)\right], \tag{4.4}$$

$$\omega_{BS} = g/(\omega_q + \omega_r), \tag{4.5}$$

where $g(n)$ is now a coupling operator dependent on the photon number in the bosonic mode, $\omega_{BS}$ the Bloch-Siegert shift frequency and $n = a^\dagger a$. The fact that we have a qutrit interacting with two modes does not allow a generalisation of such a perturbative treatment for both modes. For the CPB-like qutrit, we could neglect the third level due to its much higher frequency $\Omega_{ef} > \Omega_{ge}$. However, we cannot eliminate both counter-rotating terms by performing the transformations $e^{S_1}e^{S_2}He^{-S_2}e^{-S_1}$, where $S_i = \gamma_i(a_i\sigma_{ge} + a_i^\dagger\sigma_{eg})$ and $\gamma_i = \eta_i g/(\omega_i + \Omega_{ge})$ as $\left[e^{S_1}, e^{S_2}\right] \neq 0$. Moreover, we do not gain anything by doing only one transformation because, while eliminating counter-rotating terms in the interaction of one mode with the qubit, we would be adding a three-body interaction term coupling the two bosonic modes and the qubit proportional to $t_{ge}\gamma_1(a_0^\dagger - a_0)(a_1 + a_1^\dagger)(\sigma_{ee} - \sigma_{gg})$.

### 4.1.3 Considerations on the DSC regime

Similar three level systems coupled to two bosonic modes have been already discussed in [61, 62]. The main difference between our model and those of [61, 62], is that in our model both transitions are coupled to both modes. In [15] the DSC regime of the QRM was presented for the first time and two important features were described: (i) the independent parity chains and (ii) the use of a coherent state basis for an approximation of the dynamics. Here we are going to briefly review the basic results of that paper. The key element necessary to understand the DSC regime is the parity operator

$$\Pi = -\sigma_z(-1)^{n_a} = (|g\rangle\langle g| - |e\rangle\langle e|)(-1)^{n_a},$$

with eigenvalues $\Pi|p\rangle = p|p\rangle$ and $p = \pm 1$. These parity values split the relevant Hilbert space of the QRM into two unconnected subspaces

$$\begin{aligned} &|g0_a\rangle \leftrightarrow |e1_a\rangle \leftrightarrow |g2_a\rangle \leftrightarrow |e3_a\rangle \leftrightarrow ...(p = +1), \\ &|e0_a\rangle \leftrightarrow |g1_a\rangle \leftrightarrow |e2_a\rangle \leftrightarrow |g3_a\rangle \leftrightarrow ...(p = -1). \end{aligned} \tag{4.6}$$

Using this, the parity basis $|p, n_b\rangle$ was introduced, where $b^\dagger b|n_b\rangle = n_b|n_b\rangle$ and $b = \sigma_x a$ so that $b|p, n_b\rangle = \sqrt{n_b}|p, n_b - 1\rangle$. Using this basis, the Rabi Hamiltonian (4.2) can be rewritten as

$$H_R = \hbar\omega_r b^\dagger b + \hbar g\left(b + b^\dagger\right) - \hbar\frac{\Omega_q}{2}(-1)^{b^\dagger b}\Pi, \tag{4.7}$$

The term $\hbar g\left(b + b^\dagger\right)$ can be removed by changing to the basis $D(-\beta_0)|p, n_b\rangle$, with $D(\beta_0) = e^{\beta_0 b^\dagger - \beta_0^* b}$ and $\beta_0 = g/\omega$. In the limit of $\Omega_q = 0$ the Hamiltonian (4.7) can be exactly diagonalized, with eigenenergies $E^{\beta_0}_{p,n_b}/\hbar = \omega_r n_b - g^2/\omega_r$.

In our Hamiltonian (4.1) with the off-diagonal coupling configuration, we can similarly define a parity operator $\Pi = (|g\rangle\langle g| - |e\rangle\langle e| + |f\rangle\langle f|)(-1)^{n_0+n_1}$ that splits the Hilbert space into two different parity chains

$$\begin{aligned} &|g00\rangle \leftrightarrow |e10\rangle \leftrightarrow |g11\rangle \leftrightarrow |e01\rangle \leftrightarrow |f11\rangle \leftrightarrow ...(p = +1), \\ &|e00\rangle \leftrightarrow |g10\rangle \leftrightarrow |e20\rangle \leftrightarrow |f21\rangle \leftrightarrow |e22\rangle \leftrightarrow ...(p = -1). \end{aligned} \tag{4.8}$$

For the CPB-like system, where the second qutrit transition is quite far off-resonance with the first transition and mode, the system can be effectively reduced to a two-level system coupled to the two modes. In the transmon-like system, it is however of great importance to consider the three levels and we will therefore consider the chains in (4.8). Nevertheless, we will restrict our focus to a numerical study taking as reference the DSC article [15].

## 4.2 Energy spectra and populations

In order to understand the two systems that we have proposed, we perform a numerical diagonalization of the Hamiltonian (4.1) $H|\Psi_k\rangle = E_k|\Psi_k\rangle$, with the off-diagonal coupling explained in the section above. We fix all parameters except for the couplings $s_{ij}$ and $t_{ij}$, and plot the difference of energies $E_k - E_0$ with respect to that of the first eigenstate, see Fig. 4.1. There we can see that when the coupling becomes $s_{ij}/\omega_0 \gtrsim 1.2$, the lowest eigenstates become $2m$-fold degenerate ($m \in \mathbb{N}$). In particular, the first six are grouped in pairs, both for the CPB-like and transmon-like qutrit systems. This is the region known as the DSC regime [15]. In the range of ($0.1 < s_{ij} < 1.2$), non-trivial crossing points and energy splitting between the eigenstates

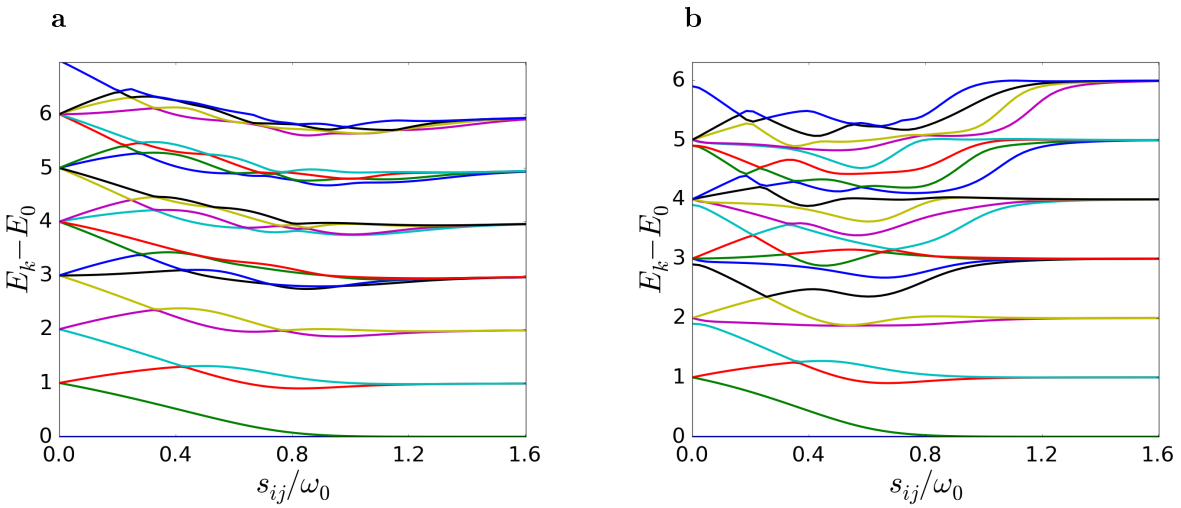


Figure 4.1: Energy spectrum of the Hamiltonian (4.1) with $\omega_0 = \Omega_{01} = \beta_0 = 1$, (**a**) $\Omega_{12} \approx 8.5\Omega_{01}$ and (**b**) $\Omega_{12} \approx 0.90\Omega_{01}$. Both systems tend to a degeneracy of energy states; the so called DSC regime, $s_{ij}/\omega_0 \gtrsim 1.2$. Between the perturbative USC and DSC regime ($0.1 < s_{ij} < 1.2$) there is a region of non-trivial crossing points and energy splitting between the eigenstates; also known as the dark zone [63]. The eigenstates of both systems braid together in groups of even number of states, but more complex crossings occur in the dark zone of the transmon-like qutrit.

occur. For the CPB-like system, where the third level is way off resonant with the modes, the dark zone [63] has a similar braiding shape as the one of the QRM [25].

Bare fock states populations of the four low-energy eigenstates at $s_{ij}/\omega_0 = 1.6$ (DSC regime) of the transmon-like system are shown in Fig. 4.2. The projections of the ground and first excited states $|\Psi_{0,1}\rangle$ to the bare fock state basis of the first bosonic mode $|n_0\rangle$ have almost Gaussian probability distributions $P^k_{n_0} = |\langle\Psi_k|n_0\rangle|^2$, whereas for the second and third excited states $P^k_{n_0}$ have two-Poisson like components. Repeating the calculation of populations for the second bosonic mode $P^k_{n_1}$, we have found that this mode can not be neglected in the DSC limit (not shown in Fig. 4.2).

## 4.3 Collapse and revivals of populations

In the DSC regime of the quantum Rabi model it has been shown that in the limit where the frequency of the qubit is $\Omega_q = 0$, free Hamiltonian dynamics of simple bare states can be analytically solved. In particular, in [15] they calculated the evolution of the initial state $|\Psi(0)\rangle = |+, 0_b\rangle = |g, 0_a\rangle$. Using the change of basis discussed in Sec. 4.1.3 one finds

$$\begin{aligned} |\Psi(t)\rangle &= D^\dagger(\beta_0) e^{-i(\omega_r b^\dagger b - g^2/\omega_r)t} D(\beta_0)|+, 0_b\rangle = U(t, \Omega_q)|\Psi(0)\rangle \\ &= e^{i(g^2/\omega_r)t - i(g/\omega_r)^2 sin(\omega_r t)}|+, \beta(t)\rangle, \end{aligned} \tag{4.9}$$

with $\beta(t) = \beta_0\left(e^{-i\omega t} - 1\right)$ the amplitude of the coherent state. The revival probability of the initial state is then

$$P_{+0_b}(t) = |\langle\Psi(0)|\Psi(t)\rangle|^2 = e^{-|\beta(t)|^2}. \tag{4.10}$$

In Figs. 1(b,c) of [15] we can see perfect revivals of the $|+, 0_b\rangle$ and $|+, 2_b\rangle$ states respectively at times $t = k(2\pi/\omega_r)$ with $k \in \mathbb{N}$. We have looked for similar behaviour in our systems, both in the DSC regime and in the dark zone between the USC and the DSC regimes.

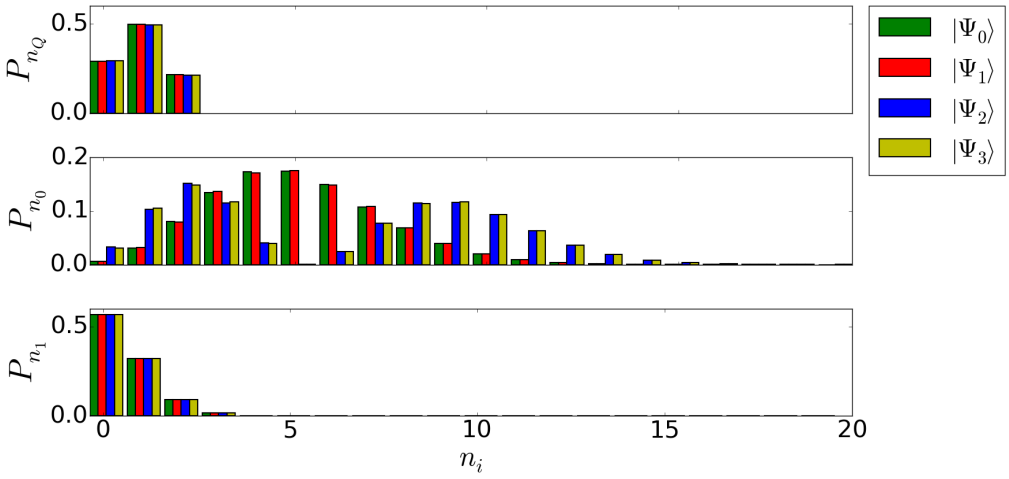


Figure 4.2: Population of the ground state and first excited state of (4.1) with $\omega_0 = \Omega_{01} = \eta_0 = 1$ $\Omega_{12} \approx 0.90\Omega_{01}$ and $s_{ij}/\omega_0 = 1.6$. The first mode with $\omega_0$ has almost Gaussian statistics for the ground and first excited states $P^k_{n_0} = |\langle\Psi_k|n_0\rangle|^2$, and close to two-Poisson components in the second and third excited states $|\Psi_{2,3}\rangle$.

### 4.3.1 Transmon-like qutrit

In the transmon-like qutrit described in Sec. 4.1, we have found that the populations of initial states of the type $|\Psi(0)\rangle = |e, n_0, 0\rangle$, with low fock state number $n_0$ in the resonator mode, collapse and revive very much like the ones described in [15]. See Fig. 4.3 for the revival probability of initial states with $n_0 = 0, 1$, $P(t) = |\langle\Psi(0)|\Psi(t)\rangle|^2$. In particular, note that the initial states correspond to different parity chains and yet their initial populations collapse and revive. It is remarkable how the case where $\Omega_{ef} \approx 0.9\Omega_{ge}$ (solid black) and the one where $\Omega_i = 0\,\forall i \in \{g, e, f\}$ (green slashed lines) agree. Furthermore, the initial population in the first excited state of the qutrit collapses into a constant value around $P_e \approx 0.5$, while the ground and second excited states share the rest of the population during this process, $P_g \approx 0.27$ and $P_f \approx 0.23$ respectively, see Fig. 4.4. The degenerate three level system coupled to one bosonic mode in the DSC regime should behave extremely similarly to this one, and it is expected to be analytically solvable.

### 4.3.2 CPB-like qutrit

As the the CPB-like qutrit is very similar to a qubit, collapses and revivals within the DSC regime become even clearer than in the transmon-like system. Therefore, we have investigated whether this system has some collapse and revival behaviour in the much less intuitive region of the dark zone $0.1 < s_{ge}/\omega_0 < 1$. We can see in Fig. 4.5(a) an evolution of an initial coherent state of amplitude $\beta = 2$ in the first bosonic mode $|\Psi(0)\rangle = |g, \beta, 0\rangle$. Perfect collapses and half revivals at about $t = k(2\pi/\omega_0)$, for $s_{ge}/\omega_0 = 0.3$, can be seen in the black solid line, whereas green slashed lines show almost perfect revivals for the limit case with a degenerate qutrit $\Omega_i = 0$. The latter coincide with rotations of the reduced density matrix $\rho_0(t) = Tr_{Q,1}\left[|\Psi(t)\rangle\langle\Psi(t)|\right]$ in the phase space, which can be seen in the Wigner function $W(\alpha)$ [64] of $\rho_0(t)$ in Fig. 4.5(b), where $Tr_{Q,1}[\cdot]$ represents the partial trace with respect to the qutrit and the second bosonic mode.

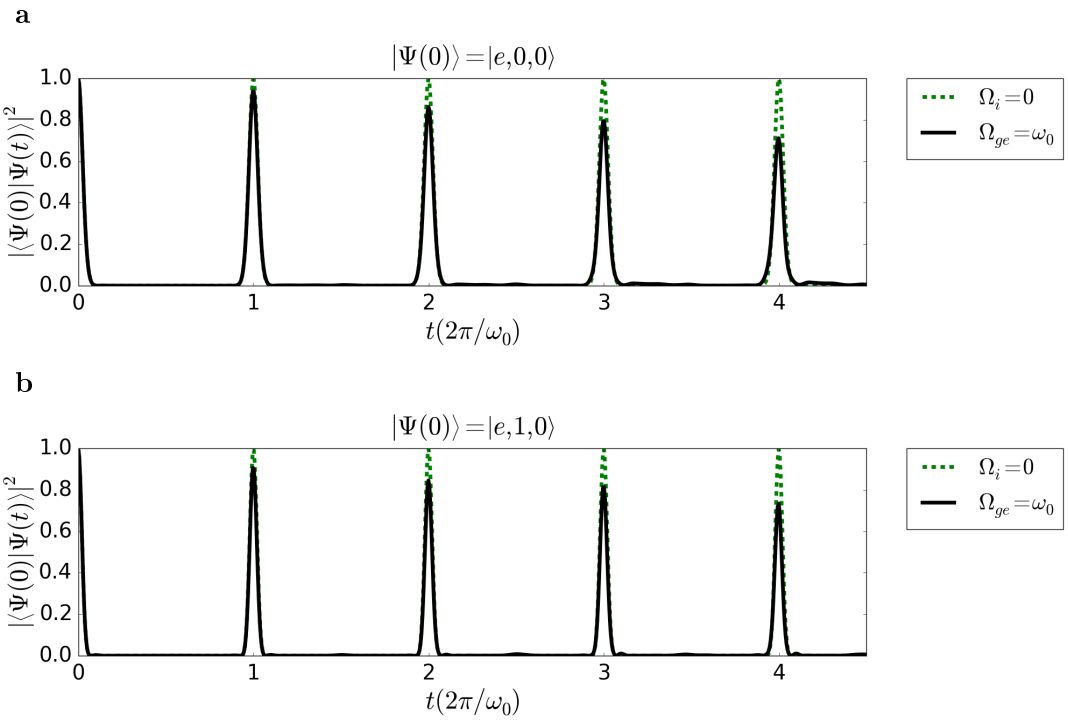


Figure 4.3: Collapse and revivals of an initial state (**a**) $|\Psi(0)\rangle = |e,0,0\rangle$ and (**b**) $|\Psi(0)\rangle = |e,1,0\rangle$ with $\Omega_{ge} = \omega_0$, $\Omega_{ef} \approx 0.9\Omega_{ge}$ and $s_{ij} = 1.6\omega_0$ (solid lines). The limit case where $\Omega_i = 0$, $\forall i \in \{g,e,f\}$ is plotted in green slashed lines.

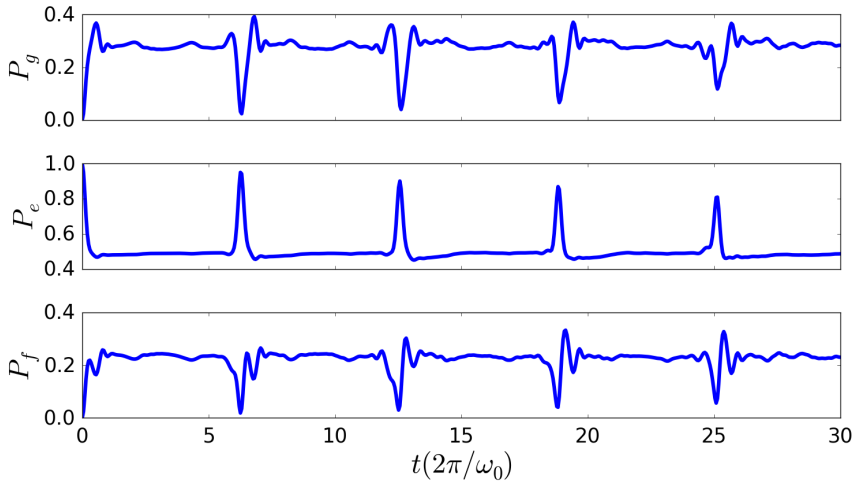


Figure 4.4: Time evolution of the population in the transmon-like qutrit with initial state $|\Psi(0)\rangle = |e,0,0\rangle$, $\Omega_{ge} = \omega_0$, $\Omega_{ef} \approx 0.9\Omega_{ge}$ and $s_{ij}/\omega_0 = 1.6$. Population in the first excited state of the qutrit remains constant to almost $P_e \approx 0.5$ for the whole collapsing time. The rest of the population is shared between the ground ($P_g \approx 0.27$) and second excited state ($P_g \approx 0.23$). Population gets slowly mixed over time and revivals blur over time.

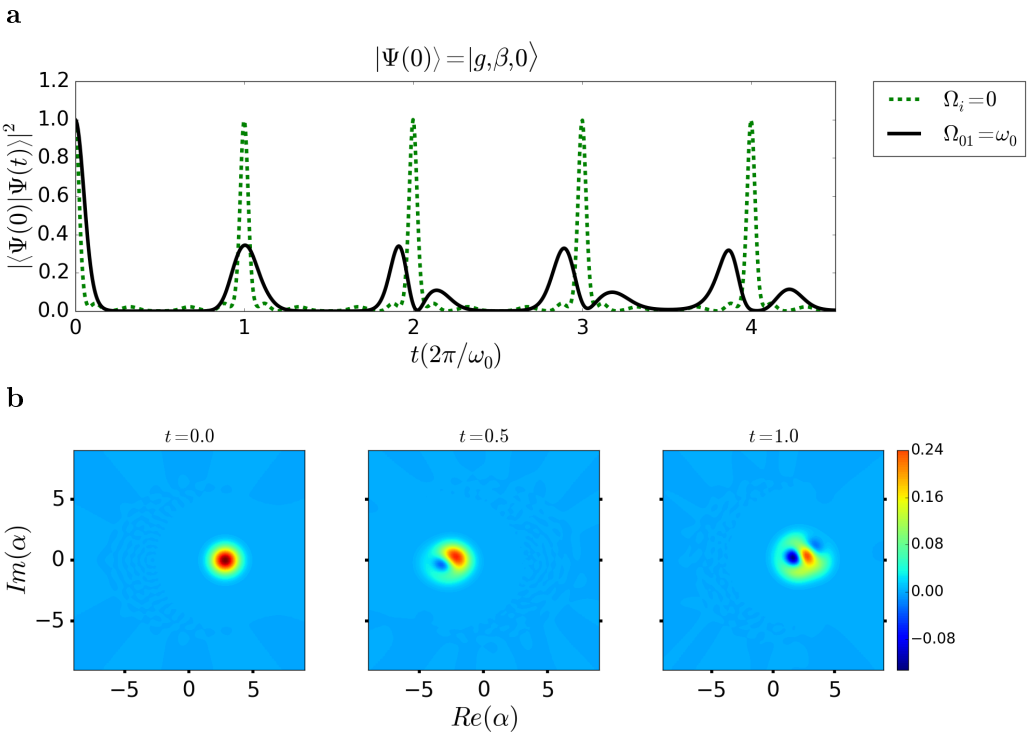


Figure 4.5: (a)Unitary free evolution of an initial coherent state in the first bosonic mode $|\Psi(0)\rangle = |g, \beta = 2, 0\rangle$ with $s_{ge}/\omega_0 = 0.3$. Full collapses and half revivals at about $t = k\,(2\pi/\omega_0)$ can be seen in black solid line. Green slashed lines show perfect revivals for the limit case with a degenerate qutrit $\Omega_i = 0$. (b) Wigner function $W(\alpha)$ of the reduced density matrix $\rho_0(t)$ , with time in units of $(2\pi/\omega_0)$. It can be observed that the initial coherent state population mixes into two very close components with opposite maximum values at the pseudo-revival time $t = k\,(2\pi/\omega_0)$.

## 4.4 Realizability with superconducting circuits

We finish the chapter by performing similar state evolutions in the qutrit-two-mode system, with the transmon-like coupling configuration that we introduced in Sec. 4.1.1. We recall the Hamiltonian of the system (4.1), with $g_{ij} = \langle i|\hat{n}_J|j\rangle$ and $\hat{n}_J$ the Cooper-pair number operator of an associated CPB circuit with Hamiltonian

$$H_{CPB} = 4E_C(\hat{n}_J - n_g)^2 - E_J\cos(\hat{\varphi}_J), \tag{4.11}$$

which written in its eigenvector basis $|i\rangle$ becomes $H_{CPB} = \hbar\sum_{i=0}^{2}\Omega_i\sigma_{ii}$. We have assumed the charge bias to be at the sweet spot $n_g = 0.5$ where these systems are more resilient to charge noise. In Fig. 3.3(b) it was shown that as $E_J/E_C$ increases, the coupling parameters $g_{ij}$ tend to a constant value in the diagonal components $g_{ii} \to n_g$. At the same time, the couplings of the non-nearest neighbour states tend to zero $g_{i,i\pm j} \to 0$ with $j \neq 1$ and the rest of the coupling terms have different values $g_{i,i\pm1} \neq g_{j,j\pm1}$ with $i \neq j$. The Hamiltonian (4.1) can therefore be rewritten as

$$H = \hbar\sum_{i=0}^{2}\Omega_i\sigma_{ii} + \sum_{n=0,1}\hbar\omega_n a_n^\dagger a_n + \hbar\sum_{i=j\pm1}g_{ij}\sigma_{ij}\sum_n\eta_n\left(a_n + a_n^\dagger\right) + \sum_n n_g\mathbb{1}_Q\eta_n\left(a_n + a_n^\dagger\right), \tag{4.12}$$

where $\mathbb{1}_Q = \sum_{i=0}^{2} \sigma_{ii}$. Performing the simple Bogoliubov transformation $a_n \to b_n - n_g\eta_n/\omega_n$, $a_n^\dagger \to b_n^\dagger - n_g\eta_n/\omega_n$ would seem to remove the diagonal coupling elements in the Hamiltonian

$$H = \hbar\sum_{i=0}^{2}\Omega_i\sigma_{ii} + \hbar\sum_{i=j\pm1}^{2} g_{ij}\sum_n \delta_n\sigma_{ij} + \sum_{n=0,1}\hbar\omega_n b_n^\dagger b_n + \hbar\sum_{i=j\pm1} g_{ij}\sigma_{ij}\sum_n \eta_n\left(b_n + b_n^\dagger\right), \quad (4.13)$$

where $\delta_n = -n_g\eta_n^2/\omega_n$ and the constant energy shift $\hbar\sum_n (n_g\eta_n)^2/\omega_n$ has been removed. However, note that the qutrit subsystem is no longer in diagonal form. The inefficiency of this method motivates us to continue performing our numerical simulations with the full Hamiltonian.

### 4.4.1 Transmon-like qutrit

As was pointed out before, the transmon-like qutrit energy levels can be realised with a transmon working at $E_J/E_C = 15$, which is close to its maximum of anharmonicity. With such a ratio of energies, the coupling parameters become $g_{ii} = 0.5$, $g_{ge} = 0.783$ and $g_{ef} = 1.01$ and the rest can be neglected. Full collapses and revivals of the initial state $|\Psi(0)\rangle = |e,0,0\rangle$ populations, at the DSC regime parameter values of $s_{ge} \equiv \beta_0 g_{ge} = 1.6\omega_0 g_{ge}$, are plotted in Fig. 4.6, where solid black lines are the collapses and revivals of the transmon-like coupling configuration, whereas the red dashed line corresponds to the diagonal evolution of Fig. 4.3(a) with the off-diagonal coupling configuration. In Fig. 4.7, Wigner functions of the reduced density matrix

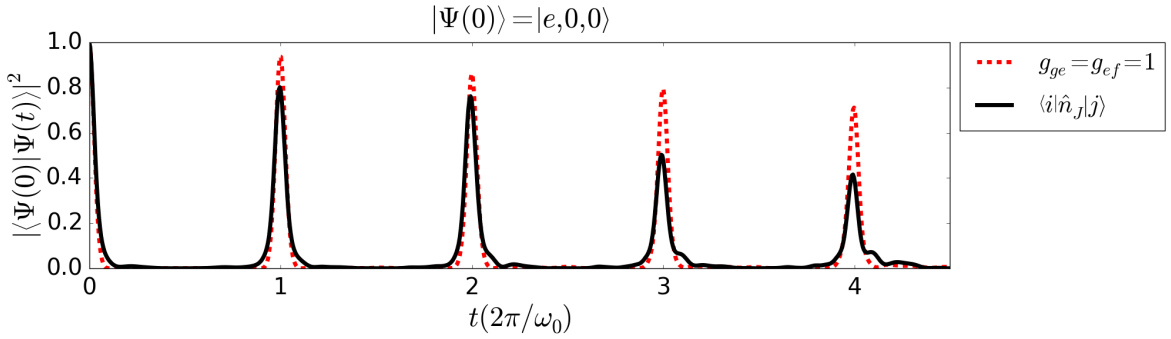


Figure 4.6: Collapse and revivals of the populations of the initial state $|\Psi(0)\rangle = |e,0,0\rangle$ with transmon-like coupling $s_{ij} = \eta_0 g_{ij} = 1.6\omega_0 g_{ij}$ (black solid line) and the diagonal coupling case of Fig. 4.3 with $g_{ge} = g_{ef} = 1$ (red dashed line) and $\eta_0 = 1.6\omega_0$.

$\rho_0(t) = Tr_{Q,1}\left[|\Psi(t)\rangle\langle\Psi(t)|\right]$, display how the $|0\rangle_0$ fock state in the first bosonic mode splits into two coherent state components, actually with similar cat state-like components in each qutrit level (not shown in the figure) that cycle around the phase space to revive again at $t = 2\pi/\omega_0$. Figure (a) corresponds to the diagonal case shown in Fig. 4.3, whereas figure (b) corresponds to the transmon-like coupling configuration.

### 4.4.2 CPB-like qutrit

The CPB-like qutrit could be realised with a ratio of $E_J/E_C = 1$, where the second transition is very far off-resonance with the first one. The couplings for that energy ratio become $g_{ii} = 0.5$, $g_{ge} = -0.504$ and $g_{ef} = -0.07$, which means that not only the second qutrit transition is way off-resonance $\Omega_{ef} \approx 8.5\Omega_{ge}$, but its transition is weakly coupled to the bosonic modes. This means that here, the qubit approximation becomes even better. Again, we have searched for initial coherent state ($|\Psi(0)\rangle = |g,\beta = 2,0\rangle$) populations to collapse and revive in the first

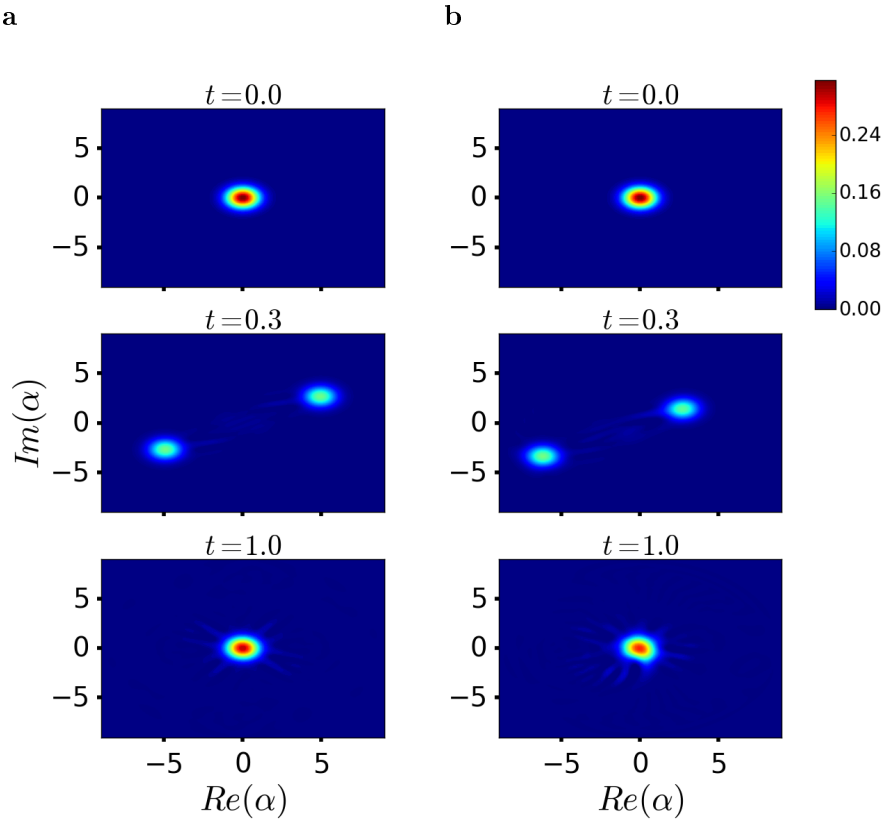


Figure 4.7: Wigner functions of the reduced density matrix $\rho_0(t)$ for the initial state $|\Psi(0)\rangle = |e,0,0\rangle$ with: (a) the diagonal coupling explained in Sec. 4.3.1, and (b) the transmon-like qutrit with capacitive coupling, with time in units of $(2\pi/\omega_0)$. The $|0\rangle_0$ fock state in the first bosonic mode splits into two coherent state components (cat state-like) that cycle around the phase space. Almost perfect revival at $t = 2\pi/\omega_0$ can be seen in the diagonal configuration.

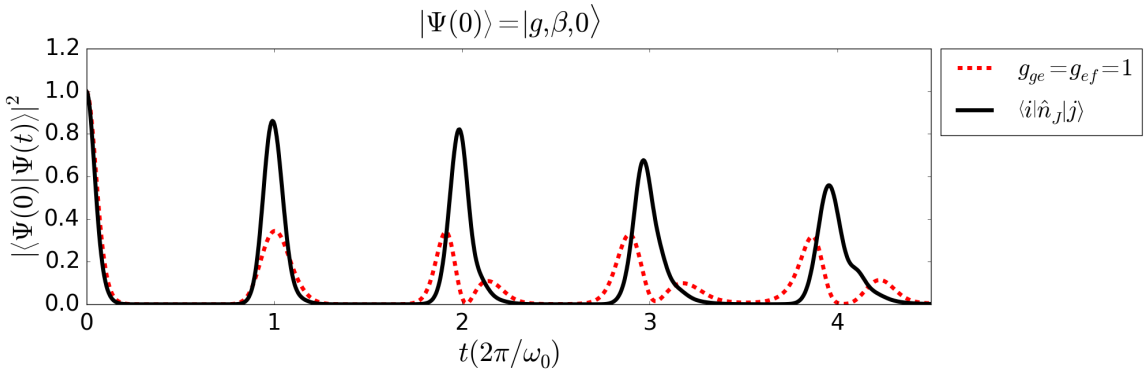


Figure 4.8: Collapse and revivals of the populations of the initial state $|\Psi(0)\rangle = |g,\alpha,0\rangle$ with $\alpha = 2$ the amplitude of the coherent state. Black solid line is the evolution for the transmon-like coupling configuration at $s_{ij} = 0.5\omega_0 g_{ij}$ (best collapses and revivals found in the dark zone for this state). Red dashed line is the evolution with the off-diagonal coupling configuration at $s_{ij} = 0.3\omega_0$ of Fig. 4.5(a).

bosonic mode when the coupling to the qutrit is in the dark zone $s_{ge} = 0.5\omega_0 g_{ge} \approx 0.25\omega_0$. See the black solid line in Fig. 4.8. A comparison with the above evolution in Fig. 4.5(a) is shown in the red dashed line.

To summarise, in this chapter we have seen the possibility of observing a typical features of the DSC regime, in more realistic superconducting qubit implementations. Furthermore, with the current evolution of the superconducting technologies, we expect such observations in laboratories with transmon qubits in the near future.

# Chapter 5

# Conclusions and outlook

In this thesis, we have aimed at (i) describing transmon qubits capacitively coupled to transmission line resonators at the ultrastrong coupling regime and (ii) predict collapses and revivals of the populations of initial states in the USC and DSC regimes of qutrit subsystems coupled to multimode resonators.

In chapter 2, we reviewed the basic theory of superconducting circuits and circuit quantum electrodynamics, with a detailed analysis on the quantization procedure of transmission line resonators and the Cooper-pair Box. We also saw that Kirchhoff's laws at the end of the transmission line resonator (boundary conditions) can be also generally obtained applying the calculus of variation to the action of the associated Lagrangian.

In chapter 3, we have revisited the transmon qubit making a special emphasis on the quantization procedure and we have pointed out the parameters of the original model that must be engineered in order to reach the USC regime. A new microscopic circuit model has been fully quantized in order to explore the possibility of reaching the USC and DSC regimes. This model has been experimentally verified by fitting its Hamiltonian parameters to the heuristic model describing the experimental dataset shared by the group of Gary Steele. The heuristic model describing the energy spectrum of the dataset has been also analysed, but no special features having found where counter-rotating terms play a significant role. In any case, both models agreed that a transmon qubit in the non-resonant USC regime has been experimentally realised. The circuit model has been able to fit the heuristic model to a very high extent using as parameters very close to their original design. Thus, it would be interesting to investigate the possibility of using it for designing future experiments. In that line, a thorough comparison between this model and a blackbox approach would have an important value in terms of predictability. It would be then crucial to study how bigger capacitances would agree with the model when stronger border effects might start to pop up.

In chapter 4, we have studied an extended version of the quantum Rabi model, where the qubit has been replaced by a three-level system, and where we have added a second bosonic mode with frequencies and couplings corresponding to those of a second harmonic in a transmission line resonator. We have explored two kind of qutrit species: (i) a transmon-like qutrit where the second transition is very similar to the first energy transition, and (ii) a CPB-like qutrit where the second transition is far off-resonance. It has been explored the USC and DSC regimes between the first transition of the qubit and the first bosonic mode frequency, where the latter was laid on resonance for both qutrit configurations. It has been tried to do perturbative analyses for both regimes but symmetry problems have been encountered, e.g. removing counter-rotating terms for all transitions is not possible in the USC regime. Parity chains in the DSC regime with the two-mode-qutrit model were found, but no further analytical study could be made. Collapse and revivals of populations of initial states have been found not only

in the DSC regime (for both qutrit types although only showed in the transmon-like), but also in the USC regime for the CPB-like qutrit with capacitive coupling. That final result shows that in the dark zone between the USC and DSC regime, there could be interesting ranges of the coupling parameter where non trivial states could be used for processing tasks.

Summarising, in this thesis we have explored different models for describing a transmon qubit coupled to bosonic modes in a resonator, and a new proposed circuit model has proven (up to great extent) to describe a new experimental realisation, where the non-resonant USC regime was achieved. On the other hand, a typical DSC feature of the quantum Rabi model has been observed in an extended version with a more realistic superconducting qutrit-two-mode structure, not only in the DSC regime but also in the dark zone. Thus, this work opens several research lines, among which, the most prominent one is the use of a transmon qubit in the USC regime and beyond it as a new tool for quantum computation. Moreover, we foresee the use of transmission line resonators ultrastrongly coupled to transmon qubits to do digital-analog quantum simulations of quantum field theories, where exotic curvatures of space-time could be mapped into transmission line geometries.

# Appendix A

# Sturm-Liouville eigenvalue problem

In this appendix, we explicitly calculate some of the steps missing in the quantization procedure of the new circuit model in Sec. 3.2.

## A.1 Wave numbers $k_n$ and normalisation constants $A_n$

The eigenvalue problem set up by Eqs. (3.19)-(3.21) accepts as solution

$$u_n(x) = A_n \sin(k_n x), \quad 0 \leq x < l, \tag{A.1}$$

which, introduced in (3.21) gives the transcendental equation

$$\frac{C_0}{C_g k_n} = \tan(k_n l). \tag{A.2}$$

This Sturm-Liouville-like problem is associated with a symmetric self-adjoint operator [46] (with real eigenvalues) and therefore $k_n$ can only be either real or purely imaginary. It is trivial to check that if $k_n$ where purely imaginary then Eq. (3.25) would become $-C_0/C_g k_n = \tanh(k_n l)$, which clearly has no solution. Thus, we can conclude that $k_n$ has to take real values. This equation can be numerically solved to find the wave numbers and frequencies of the normal modes with for example the Newton-Raphson method. However, from a pictorial solution, see Fig. A.1, we can easily appreciate that modes with big wave number tend to the solution $k_n \to n\pi/l + \epsilon_n$, see below Sec. A.3 to see the scaling of $\epsilon_n$. On the other hand, if the ratio $C_g/C_0 l$ is small enough, the first modes will be close to $k_n \approx (2n+1)\pi/2l$.

Had we had a voltage source bias at the beginning of the transmission line ($x = 0$), the boundary condition of Eq. (3.21) would change to $\Phi(0,t) = V_g t$. Thus, we would have to add the constant mode with wave number and frequency $k_{DC} = \omega_{DC} = 0$ (the transcendental Eq. (A.2) does not apply here), and envelope $u_{DC}(x) = 1$, in order for the eigenfunction to be normalised according to Eq. (3.22). Using (3.18), we could extract this dc component $\psi_{DC}(t) = V_g t$ of the flux fields $\Phi(x,t) = \psi_{DC}(t) + \sum_n u_n(x)\psi_n(t)$. Finally, $\psi_{DC}(t)$ could be incorporated in the definition of the flux variable of the Josephson junction $\phi_J \to \phi_J + \psi_{DC}$, and after perfoming the Legendre transformation arrive at Eq. (3.35).

With the transcendental equation A.2, we can now find the normalisation constant for each mode $A_n$ as a function of $C_\Sigma$ setting $n = m$ in Eq. (3.22)

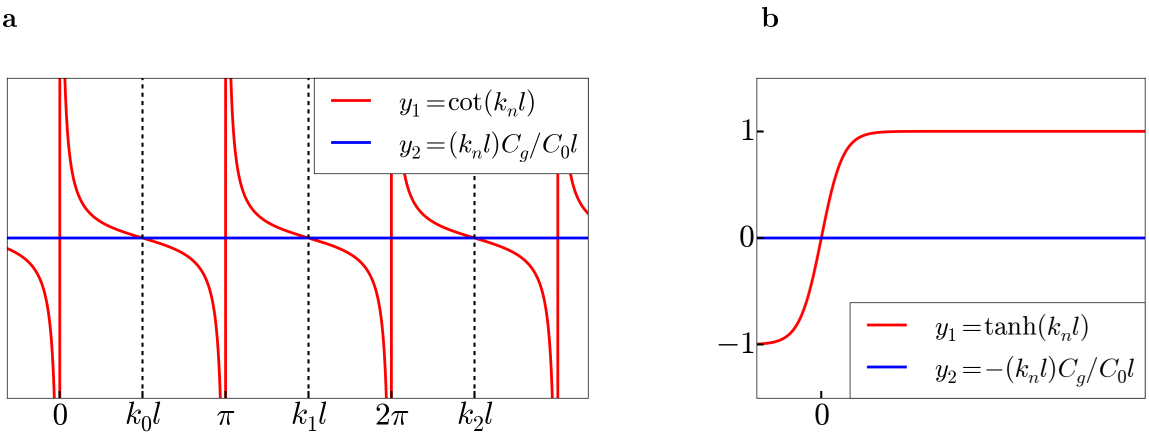


Figure A.1: (**a**) Pictorial solution of the transcendental equation A.2 with ratio $C_g/C_0 l = 0.04$ (similar to the one that the circuit model requires to fit the real experiment of Sec. 3.3). Values of $k_n l$ are found where lines $y_1$ and $y_2$ intersect. It can be appreciated, that such a small ratio yields small wave numbers very close to $k_n \approx (2n+1)\pi/2l$, whereas any ratio will force $k_n \to n\pi/l$ with $n \to \infty$ . (**b**) No solution for pure imaginary wave numbers $k_n$.

$$\int_0^l dx\, C_0 u_n^2(x) + C_g u_n^2(l) = A_n^2 \left( C_0 \int_0^l dx \sin^2(k_n x) + C_g \sin^2(k_n l) \right) \tag{A.3}$$

$$= A_n^2 \left( C_0 (\frac{l}{2} - \frac{\sin(2k_n x)}{4k_n}) + C_g \sin^2(k_n l) \right) \tag{A.4}$$

$$= A_n^2 \left( \frac{1}{2}(C_0 l - C_g \sin^2(k_n x)) + C_g \sin^2(k_n l) \right) \tag{A.5}$$

$$= \frac{A_n^2}{2} \left( C_0 l + \frac{C_g C_0^2}{C_0^2 + (C_g k_n)^2} \right) = \chi_n, \tag{A.6}$$

where to go from the second to the third line we have made use of the transcendental equation. Finally, imposing this result to Eq. (3.23) we get the final normalisation condition for the amplitudes $A_n$

$$\chi_n = \frac{A_n^2}{2} \left( C_0 l + \frac{C_g C_0^2}{C_0^2 + (C_g k_n)^2} \right) \iff \int_0^l dx\, C_0 + C_g = C_0 l + C_g = C_\Sigma, \tag{A.7}$$

and so

$$A_n = \sqrt{2 C_\Sigma} \left( C_0 l + \frac{C_g C_0^2}{C_0^2 + (C_g k_n)^2} \right)^{-1/2}. \tag{A.8}$$

We note here that as $k_n$ grows linearly and monotonically with $n$, $A_n$ is upper bounded.

## A.2 Lagrangian derivation

Using the above orthonormality condition (3.22) we can now rewrite our Lagrangian (3.14) in the basis $\{u_n(x)\}$. Letting $\mathcal{L} = \frac{1}{2}(\mathcal{L}_K - \mathcal{L}_P + \mathcal{L}_{int} + \mathcal{L}_{CPB})$ and dropping for simplicity the time parameter of the functions $\psi_n$ and $\phi_J$ we have

$$\mathcal{L}_K = \int_0^l dx C_0 \left(\dot{\Phi}(x,t)\right)^2 \tag{A.9}$$

$$= \int_0^l dx C_0 \sum_{n,m} \dot{\psi}_n \dot{\psi}_m u_n(x) u_m(x) \tag{A.10}$$

$$= \sum_{n,m} \dot{\psi}_n \dot{\psi}_m \int_0^l dx C_0 u_n(x) u_m(x) \tag{A.11}$$

$$= \sum_{n,m} \dot{\psi}_n \dot{\psi}_m \left(C_\Sigma \delta_{nm} - C_g u_n(l) u_m(l)\right) \tag{A.12}$$

$$\mathcal{L}_P = \int_0^l dx \frac{1}{L_0} \left(\Phi^{'}(x,t)\right)^2 \tag{A.13}$$

$$= \int_0^l dx \frac{1}{L_0} \sum_{n,m} \psi_n \psi_m u_n^{'}(x) u_m^{'}(x) \tag{A.14}$$

$$= \sum_{n,m} \psi_n \psi_m \left( \left[ \frac{u_n^{'}(x) u_m^{'}(x)}{L_0} \right]_0^l - \int_0^l dx \frac{u_n^{''}(x)}{L_0} u_m(x) \right) \tag{A.15}$$

$$= \sum_{n,m} \psi_n \psi_m \omega_n^2 \left( C_g u_n(l) u_m(l) + \int_0^l dx C_0 u_n(x) u_m(x) \right) \tag{A.16}$$

$$= \sum_{n,m} \psi_n \psi_m \omega_n^2 C_\Sigma \delta_{nm} = C_\Sigma \sum_{n,m} \psi_n^2 \omega_n^2 \tag{A.17}$$

$$\mathcal{L}_{int} = C_g \left(\dot{\Phi}(l,t) - \dot{\phi}_J\right)^2 \tag{A.18}$$

$$= C_g \sum_{n,m} \dot{\psi}_n \dot{\psi}_m u_n(l) u_m(l)$$

$$-2C_g \sum_n \dot{\psi}_n u_n(l) \dot{\phi}_J + C_g \dot{\phi}_J^2 \tag{A.19}$$

and summing all the terms we arrive to the Lagrangian

$$\mathcal{L} = \sum_n \frac{C_\Sigma}{2} \dot{\psi}_n^2 - \frac{1}{2L_n} \psi_n^2 - C_g \dot{\psi}_n u_n(l) \dot{\phi}_J + \frac{(C_J + C_g)}{2} \dot{\phi}_J^2 + E_J \cos\left(2\pi \phi_J / \phi_0\right). \tag{A.20}$$

## A.3 Convergence issues of the sum $\alpha_S^2$

We see from the pictorial solution of the transcendental equation (Fig. A.1) that for large $n$, $k_n l \to n\pi + \epsilon_n$, where $\epsilon_n$ is a small displacement. Under this assumption, we write the transcendental equation as

$$n\pi + \epsilon_n \approx \frac{C_0 l}{C_g} \mathrm{cotg}\left(n\pi + \epsilon_n\right) \tag{A.21}$$

$$= \frac{C_0 l}{C_g} \mathrm{cotg}(\epsilon_n). \tag{A.22}$$

Expanding the cotangent term to second order

$$n\pi + \epsilon_n = \frac{C_0 l}{C_g}\frac{1}{\epsilon_n}\left(1 - \frac{\epsilon_n^2}{3} + O\left(\epsilon_n^4\right)\right), \tag{A.23}$$

and retaining only the first order term in $\epsilon_n$ we find the approximate solution

$$\epsilon_n \approx \frac{C_0 l}{C_g n\pi}. \tag{A.24}$$

We can derive now the scaling of $k_n l$

$$k_n l \to n\pi\left(1 + O\left(\frac{1}{n^2}\right)\right). \tag{A.25}$$

On the other hand, the coupling constant $\alpha_n$ is proportional to $u_n(l) = A_n \sin(k_n l)$. We have seen in Sec. A.1 that $A_n$ is upper bounded for large $n$, while the scaling of $\sin(k_n l)$ can be calculated as

$$\begin{aligned} \sin\left(k_n l\right) &\approx \sin\left(n\pi + \epsilon_n\right) && \text{(A.26)}\\ &= (-1)^n \sin(\epsilon_n) && \text{(A.27)}\\ &\approx (-1)^n \frac{C_0 l}{C_g n\pi}. && \text{(A.28)} \end{aligned}$$

An approximate formula for the sum $\alpha_S^2$ is

$$\begin{aligned} \alpha_S^2 &= \sum_n \alpha_n^2 = \left(\frac{C_g}{\sqrt{C_\Sigma C_G}}\right)^2 \sum_n u_n^2(l) && \text{(A.29)}\\ &\approx \frac{C_g^2}{C_\Sigma C_G}\sum_{n=0}^{N} A_n^2 \sin^2(k_n l) + \left(\frac{2C_0 l}{\pi\sqrt{C_\Sigma C_G}}\right)^2 \sum_{n=N}^{\infty} A_n^2 \frac{1}{n^2} && \text{(A.30)}\\ &= \frac{C_g^2}{C_\Sigma C_G}\sum_{n=0}^{N} A_n^2 \sin^2(k_n l) + \frac{8C_0 l}{\pi C_G}\psi^{(1)}(N) && \text{(A.31)} \end{aligned}$$

where $\psi^{(m)}(z)$ is the $m^{th}$ derivative of the digamma function, and we have approximated the amplitude values by their upper bounds $A_n \approx \sqrt{2C_\Sigma/C_0 l}$. The above approximate formula is valid when we truncate the finite sum to the $N^{th}$ bosonic mode, from which $k_n l \approx n\pi + \epsilon_n$ holds. Moreover, the error done by truncating to the $N^{th}$ bosonic mode scales as $O(1/N)$ due to the asymptotic behaviour of the trigamma function $\psi^{(1)}(N)$, see [65]. In order to check the convergence of the sum, it must be further studied the limits of the asymptotic series $u_n^2(l)$, e.g. by going to higher order in perturbation theory.

# Bibliography


[1] P. Shor, *Polynomial-Time Algorithms for Prime Factorization and Discrete Logarithms on a Quantum Computer*, SIAM J. Comput. **26** (5), 1484-1509 (1997).

[2] D. S. Abrams and S. Lloyd, *Simulation of Many-Body Fermi Systems on a Universal Quantum Computer*, Phys. Rev. Lett. **79**, 2586 (1997).

[3] D. Deutsch, *Quantum Theory, the Church-Turing Principle and the Universal Quantum Computer*, Proc. R. Soc. Lond. A **400**, 97-117 (1985).

[4] J. I. Cirac and P. Zoller, *Quantum Computations with Cold Trapped Ions*, Phys. Rev. Lett. **74**, 4091 (1995).

[5] T. Byrnes et al., *Quantum simulation of Fermi-Hubbard models in semiconductor quantum-dot arrays*, Phys. Rev. B **78**, 075320 (2008).

[6] L. M. K. Vandersypen and I. L. Chuang, *NMR techniques for quantum control and computation*, Rev. Mod. Phys. **76**, 1037 (2005).

[7] D. Jaksch and P. Zoller, *The cold atom Hubbard toolbox*, Annals of Physics **315** (1), 52-79, Special Issue (2005).

[8] Y. Makhlin, G. Schön, and A. Shnirman, *Quantum-state engineering with Josephson-junction devices*, Rev. Mod. Phys. **73**, 357 (2001).

[9] R. J. Schoelkopf and S. M. Girvin, *Wiring up quantum systems*, Nature **451**, 664-669 (2008).

[10] J. Q. You and F. Nori, *Atomic physics and quantum optics using superconducting circuits*, Nature **474**, 589-597 (2011).

[11] A. Blais et al., *Cavity quantum electrodynamics for superconducting electrical circuits: An architecture for quantum computation*, Phys. Rev. A **69**, 062320 (2004).

[12] R. Barends et al., *Digitized adiabatic quantum computing with a superconducting circuit*, Nature **534**, 222-226 (2016).

[13] T. Niemczyk et al., *Circuit quantum electrodynamics in the ultrastrong-coupling regime*, Nature Phys. **6**, 772-776 (2010).

[14] M. Devoret et al., *Circuit-QED: How strong can the coupling between a Josephson junction atom and a transmission line resonator be?*, Ann. Phys. **16** (10-11), 767-779 (2007).

[15] J. Casanova, et al., *Deep Strong Coupling Regime of the Jaynes-Cummings Model*, Phys. Rev. Lett. **105**, 263603 (2010).

[16] G. Romero et al., *Ultrafast Quantum Gates in Circuit QED*, Phys. Rev. Lett. **108**, 120501 (2012).

[17] C. Sabín et al., *Extracting Past-Future Vacuum Correlations Using Circuit QED*, Phys. Rev. Lett. **109**, 033602 (2012).

[18] P. Nataf and C. Ciuti, *Protected Quantum Computation with Multiple Resonators in Ultrastrong Coupling Circuit QED*, Phys. Rev. Lett. **107**, 190402 (2011).

[19] J. Koch et al., *Charge-insensitive qubit design derived from the Cooper pair box*, Phys. Rev. A **76**, 042319 (2007).

[20] M. O. Scully and M. S. Zubairy, *Quantum Optics*, Cambridge University Press (1997).

[21] P. A. M. Dirac, *The Quantum Theory of the Emission and Absorption of Radiation*, Proc. R. Soc. Lond. A **114**, 243-265 (1927).

[22] E. M. Purcell, H. C. Torrey, and R. V. Pound, *Resonance Absorption by Nuclear Magnetic Moments in a Solid*, Phys. Rev. **69**, 37 (1946).

[23] S. Haroche and D. Kleppner, *Cavity Quantum Electrodynamics*, Phys. Today **42**, 24 (1989).

[24] A. M. Zagoskin, *Quantum Engineering: Theory and Design of Quantum Coherent Structures*, Cambridge University Press (2011).

[25] D. Braak, *Integrability of the Rabi Model*, Phys. Rev. Lett. **107**, 100401 (2011).

[26] E. T. Jaynes and F. W. Cummings, *Comparison of quantum and semiclassical radiation theories with application to the beam maser*, Proc. IEEE **51**, 89-109 (1963).

[27] J. Bourassa et al., *Ultrastrong coupling regime of cavity QED with phase-biased flux qubits*, Phys. Rev. A **80**, 032109 (2009).

[28] B. Yurke, J. S. Denker, *Quantum Network Theory*, Phys. Rev. A **29**, 1419, (1984).

[29] M. Devoret, *Quantum Fluctuations in Electrical Circuits In Quantum Fluctuations*, Les Houches, Session LXIII, 351-384 (1995).

[30] D. Pozar, *Microwave Engineering*, Wiley, 4th edition (2012).

[31] J. Ulrich, F. Hassler, *A dual approach to circuit quantization using loop charges*, arXiv:1605.02750 (2016).

[32] J. Kelly et al., *State preservation by repetitive error detection in a superconducting quantum circuit*, Nature **519**, 66-69 (2015).

[33] M. Tinkham, *Introduction to Superconductivity*, Dover Publications (2004).

[34] B. D. Josephson, *Possible new effects in superconductive tunnelling*, Phys. Lett. **1**, 251 (1962).

[35] M. Büttiker, *Zero-current persistent potential drop across small-capacitance Josephson junctions*, Phys. Rev. B **36**, 3548 (1987).

[36] V. Bouchiat et al., *Quantum coherence with a single Cooper pair*, Physica Scripta T **76**, 165-170 (1998).

[37] M. Pillai et al., *Matrix Numerov method for solving Schrödinger's equation*, Am. J. Phys. **80**, 1017 (2012).

[38] P. C. Chow, *Computer solutions to the Schrödinger equation*, Am. J. Phys. **40**, 730734 (1972).

[39] H. Paik, et al, *Observation of High Coherence in Josephson Junction Qubits Measured in a Three-Dimensional Circuit QED Architecture*, Rev. Lett. **107**, 240501 (2011).

[40] T. P. Orlando et al., *Josephson Persistent-Current Qubit*, Phys. Rev. B **60**, 15398 (1999).

[41] N. Samkharadze et al., *High-Kinetic-Inductance Superconducting Nanowire Resonators for Circuit QED in a Magnetic Field*, Phys. Rev. Applied **5**, 044004 (2016).

[42] M. R. Vissers et al., *Frequency-tunable superconducting resonators via nonlinear kinetic inductance*, Appl. Phys. Lett. **107**, 062601 (2015).

[43] D. Vion, *Lecture notes in*, Quantum Entanglement and Information Processing, Elsevier 1st Edition, 443-485 (2003).

[44] C. M. Wilson et al., *Observation of the dynamical Casimir effect in a superconducting circuit*, Nature **479**, 376-379 (2011).

[45] J. Bourassa et al., *Josephson-junction-embedded transmission-line resonators: From Kerr medium to in-line transmon*, Phys. Rev. A **86**, 013814 (2012).

[46] J. Walter, *Regular eigenvalue problems with eigenvalue parameter in the boundary condition*, Mathematische Zeitschrift December **133**, Issue 4 (1973).

[47] N. M. Sundaresan, *Beyond Strong Coupling in a Multimode Cavity*, Rev. X **5**, 021035 (2015).

[48] J. R. Johansson et al., *QuTiP: An open-source Python framework for the dynamics of open quantum systems*, Comp. Phys. Comm. **183**, 1760-1772 (2012).

[49] Figures shared in private communications by Pr. Gary Steele, Sal Brosman and Mario Gely.

[50] S. E. Nigg et al., *Black-Box Superconducting Circuit Quantization*, Phys. Rev. Lett. **108**, 240502 (2012).

[51] S. Shankar et al., *Autonomously stabilized entanglement between two superconducting quantum bits*, Nature **504**, 419-422 (2013).

[52] G. Kirchmair et al., *Observation of quantum state collapse and revival due to the single-photon Kerr effect*, Nature **495**, 205-209 (2013).

[53] L. García-Álvarez et al., *Fermion-Fermion Scattering in Quantum Field Theory with Superconducting Circuits*, Phys. Rev. Lett. **114**, 070502 (2015).

[54] C. Neuenhahn and F. Marquardt, *Quantum simulation of expanding space-time with tunnel-coupled condensates*, arXiv:1208.2255 (2012).

[55] T. Bravo et al., *Analog quantum simulation of gravitational waves in a Bose-Einstein condensate*, EPJ Quantum Technology **2**, 3 (2015).

[56] A. Baust, et al., *Ultrastrong coupling in two-resonator circuit QED*, Phys. Rev. B **93**, 214501 (2016).

[57] F. Yoshihara, et al. ,*Superconducting qubit-oscillator circuit beyond the ultrastrong-coupling regime*, arXiv:1602.00415 (2016).

[58] P. Forn-Díaz et al., *Ultrastrong coupling of a single artificial atom to an electromagnetic continuum*, arXiv:1602.00416 (2016).

[59] P. Forn-Díaz et al., *Observation of the Bloch-Siegert Shift in a Qubit-Oscillator System in the Ultrastrong Coupling Regime*, Phys. Rev. Lett. **105**, 237001 (2010).

[60] A. B. Klimov and S. M. Chumakov, *A Group-Theoretical Approach to Quantum Optics*, WILEY-VCH, Weinheim (2009).

[61] Y. Wu and X. Yang, *Effective two-level model for a three-level atom in the Ξ configuration*, Phys. Rev. A **56**, 2443 (1997).

[62] B. T. Torosov et al., *Mixed Rabi Jaynes–Cummings model of a three-level atom interacting with two quantized fields*, Opt. Comm. Vol. **346**, 110-114 (2015).

[63] F. A. Wolf et al., *Dynamical correlation functions and the quantum Rabi model*, Phys. Rev. A **87**, 023835 (2013).

[64] E. Wigner, *On the Quantum Correction For Thermodynamic Equilibrium*, Phys. Rev. **40**, 749 (1932).

[65] M. Abramowitz and I. A. Stegun, *Handbook of Mathematical Functions with Formulas, Graphs, and Mathematical Tables*, National Bureau of Standards, Applied Mathematics Series **55**, Dover Publications (1972).